Internal Waves and Mixing near the Kerguelen Plateau

AMELIE MEYER*

CSIRO Ocean and Atmosphere Flagship, and Institute for Marine and Antarctic Studies, University of Tasmania, Hobart, Tasmania, Australia

KURT L. POLZIN

Woods Hole Oceanographic Institution, Woods Hole, Massachusetts

BERNADETTE M. SLOYAN

CSIRO Ocean and Atmosphere Flagship, Hobart, Tasmania, Australia

HELEN E. PHILLIPS

Institute for Marine and Antarctic Studies, University of Tasmania, and ARC Centre of Excellence for Climate System Science, Hobart, Tasmania, Australia

(Manuscript received 20 March 2015, in final form 13 November 2015)

ABSTRACT

In the stratified ocean, turbulent mixing is primarily attributed to the breaking of internal waves. As such, internal waves provide a link between large-scale forcing and small-scale mixing. The internal wave field north of the Kerguelen Plateau is characterized using 914 high-resolution hydrographic profiles from novel Electromagnetic Autonomous Profiling Explorer (EM-APEX) floats. Altogether, 46 coherent features are identified in the EM-APEX velocity profiles and interpreted in terms of internal wave kinematics. The large number of internal waves analyzed provides a quantitative framework for characterizing spatial variations in the internal wave field and for resolving generation versus propagation dynamics. Internal waves observed near the Kerguelen Plateau have a mean vertical wavelength of 200 m, a mean horizontal wavelength of 15 km, a mean period of 16 h, and a mean horizontal group velocity of 3 cm s^{-1}. The internal wave characteristics are dependent on regional dynamics, suggesting that different generation mechanisms of internal waves dominate in different dynamical zones. The wave fields in the Subantarctic/Subtropical Front and the Polar Front Zone are influenced by the local small-scale topography and flow strength. The eddy-wave field is influenced by the large-scale flow structure, while the internal wave field in the Subantarctic Zone is controlled by atmospheric forcing. More importantly, the local generation of internal waves not only drives large-scale dissipation in the frontal region but also downstream from the plateau. Some internal waves in the frontal region are advected away from the plateau, contributing to mixing and stratification budgets elsewhere.

1. Introduction

Oceanic internal waves are ubiquitous. These waves are the result of the restoring action of buoyancy and Coriolis forces on water parcels displaced from their equilibrium position. Internal waves induce isopycnal oscillations in the ocean interior as opposed to surface gravity waves that induce oscillations of the free surface of the ocean. Internal waves are characterized by vertical length scales from a few meters to 1 km, horizontal length scales from a few meters to tens of kilometers, group velocities of 5 cm s^{-1}, amplitudes from meters to tens of meters, and periods from several minutes to several hours (Thorpe 2005; Kantha and Clayson 2000, chapter 6). Along their pathway, nonlinear interactions among the waves (wave–wave interactions), interactions

* Current affiliation: Norwegian Polar Institute, Tromsø, Norway.

Corresponding author address: Amelie Meyer, Norwegian Polar Institute, Framsenteret, 9296 Tromsø, Norway.
E-mail: amelie.meyer@npolar.no

DOI: 10.1175/JPO-D-15-0055.1

with the mean flow (wave–mean interactions), and other processes cascade the energy of internal waves to smaller scales until the energy from internal waves is dissipated. Ultimately, most of the energy of internal waves dissipates as turbulent mixing. The remaining fraction of energy is exchanged with the mean flow. While some internal waves are sufficiently nonlinear to break immediately, enhancing diapycnal mixing, many internal waves radiate away from their generation point, and their breaking contributes to the background mixing in the ocean interior. Importantly, internal waves provide a link between large-scale forcing and small-scale dissipation. The transport of momentum and energy by internal waves within the ocean is a key process in the meridional overturning circulation (Osborn 1980). Here we analyze upper ocean horizontal velocity observations from the Kerguelen Plateau region in the Southern Ocean to describe the local internal wave field and its relation to mixing. Coherent features are identified in velocity profiles from EM-APEX Argo floats and interpreted in terms of internal wave kinematics.

Perturbations of the density field that generate internal waves originate at the surface of the ocean because of the wind or at the bottom of the ocean because of tides and mean flow interaction with topography. One of the most important sources of kinetic energy in the ocean is the wind stress force τ_w exerted by the wind on the ocean surface (Wunsch and Ferrari 2004). The global net transfer of kinetic energy from the wind to the ocean is estimated to be between 7 and 36 TW (Lueck and Reid 1984; Wunsch and Ferrari 2004), most of which is directly dissipated in the surface mixed layer. A residual of some 0.3–1.2 TW is transferred to near-inertial motions (Alford 2001; Watanabe and Hibiya 2002; Scott and Xu 2009) that can propagate away from the surface mixed-layer before breaking and generating mixing at depth (Pollard and Millard 1970). Observations of near-inertial wave energy propagation from the mixed-layer into the ocean interior suggest that wind-generated inertial motions are an important part of the ocean mixing budget, particularly in the Southern Ocean (Alford et al. 2012). A second source of internal waves in the ocean is the interaction of currents with the sea floor: internal waves are generated when tidal currents and geostrophic currents flow over a topographic obstacle. Globally, the flow of the barotropic tide over topographic features such as continental slopes, shelf breaks, sills, abyssal hills, and seamounts generates more internal waves than geostrophic currents do. The estimated global tidal energy input into internal tidal waves is 1 TW, while the global energy conversion from geostrophic currents into internal waves is 0.2 TW (Nikurashin and Ferrari 2013). In the Southern Ocean geostrophic motions such as the Antarctic Circumpolar Current are very efficient at generating internal waves (Nikurashin and Ferrari 2011, 2013). Thus, the internal wave field is composed of many waves from various sources, locally generated or from the global internal wave continuum.

Despite the multiplicity of sources and boundary conditions for oceanic internal waves, there is a notion of universality of the internal wave spectrum (Munk 1981). Garrett and Munk (1975) were the first to describe and model the background oceanic internal wave field in terms of a vertical wavenumber and frequency spectrum using observations from site D in the western North Atlantic (Garrett and Munk 1972; Fofonoff 1969). The energy spectrum produced by Garrett and Munk evolved (e.g., Garrett and Munk 1975; Cairns and Williams 1976) as observational tools became more sophisticated. Ever since it was proposed, it has been used as the reference background wave field and has influenced global analyses of the internal wave field. In the past 25 years, however, regional internal wave fields have been found to vary subtly from the Garrett and Munk reference spectrum (D'Asaro and Morehead 1991; Polzin and Lvov 2011). Such variations are attributed to regional differences in the balance between nonlinearity, generation, and propagation. The tendency of internal waves to propagate large distances is one of the most ill-constrained issues that has delayed the progress of regional models of the internal wave spectrum.

The documentation of regional internal wave fields is limited. Indeed, direct observations and sampling of the spatially inhomogeneous and temporally intermittent internal wave features in four dimensions is very complex. Much of the available observations come from remote sensing of continental shelves and other shallow regions, where the vertical displacement of the thermocline due to internal waves modulates the roughness of the ocean surface (e.g., Apel et al. 1975; Fu and Holt 1982; Alpers 1985; Liu et al. 1998; Zheng et al. 2002; Susanto et al. 2005; Zhao et al. 2012; Da Silva et al. 2012). Individual internal waves are observed in echograms, acoustic backscattering, and other sonar images, as well as time series of density, velocity, and temperature variance. Globally, there are many previous observations of individual internal wave packets (e.g., Ziegenbein 1970; Liu et al. 1998; Stanton and Ostrovsky 1998). There are a few reports presenting observations of several internal wave packets (e.g., Cuypers et al. 2013), but no study has yet explored the composition of a regional internal wave

field by analyzing the characteristics of dozens of individual internal waves. Instead, previous observations of internal waves have often focused on the spectral characteristics of the internal wave field (e.g., Levine et al. 1997; Kunze et al. 2002; Fer et al. 2010; Dosser et al. 2014; Hennon et al. 2014; Martini et al. 2014).

Here we characterize 46 internal waves observed with Electromagnetic Autonomous Profiling Explorer (EM-APEX) floats. The EM-APEX floats, which sample two dimensions in a quasi-Lagrangian framework, give a unique perspective on the persistence of internal waves propagating through the mean flow. The large number of internal waves analyzed provides a quantitative framework for resolving generation versus propagation dynamics. We show that the internal wave properties are a direct result of regional dynamics. Our key finding is that in the Subantarctic/Subtropical Front, some of the internal waves and their energy are advected away from the Kerguelen Plateau, likely affecting the mixing and stratification budget in the far field. The data are described in section 2, along with aspects of the Kerguelen Plateau regional oceanography. Linear wave theory and the method to identify and analyze internal waves are described in section 3. In section 4, we present the general properties of internal waves, their regional characteristics, and their consistency with the mixing field. The implications in terms of Doppler shift and wave–mean flow interactions are discussed in section 5. We include some results from a companion paper that explores the impact of the internal wave field on local mixing characteristics (Meyer et al. 2015).

2. Data and regional oceanography

a. Observations

1) SURVEY

The observations for this study were collected north of the Kerguelen Plateau in late 2008 during the Southern Ocean Finestructure (SOFine) project. The objective of SOFine was to investigate the relation between finescale processes and the momentum balance in the Antarctic Circumpolar Current (Naveira Garabato 2009; Waterman et al. 2013; Damerell et al. 2013; Waterman et al. 2014; Phillips and Bindoff 2014; Meyer et al. 2015; Forryan et al. 2015). In this study, the analysis of the internal wave field is based primarily on data from eight EM-APEX Argo-equivalent floats. The EM-APEX floats were deployed along the ship track, on the northern edge of the Kerguelen Plateau during the SOFine oceanographic survey. Programmed to surface twice a day, they were advected eastward by the Antarctic Circumpolar Current. We use a subset of 914 profiles of temperature, salinity, pressure, and horizontal velocity from the ocean surface to 1600 m depth sampled over a period of 10 weeks in the vicinity of the Kerguelen Plateau. The profiles obtained downstream of the Kerguelen Plateau are not examined.

2) EM-APEX FLOATS

The EM-APEX profiling float is an innovative instrument that provides inexpensive, autonomous, and high-resolution observations of horizontal velocity, conductivity, temperature, and pressure. It combines a standard Teledyne Webb Autonomous Profiling Explorer float with a velocity-sensing electromagnetic subsystem. A Sea-Bird Electronics SBE-41 CTD instrument measures the temperature, salinity, and pressure. The EM-APEX electromagnetic subsystem has a compass, accelerometer, and five electrodes to estimate the magnitude of the horizontal velocity (Sanford et al. 1978) at 3-m vertical intervals.

3) QUALITY CONTROL

The temperature, salinity, and pressure data from the EM-APEX floats were quality controlled by applying the CSIRO Marine and Atmospheric Research Argo delayed-mode quality-control procedure. This was followed by extensive processing to convert the relative velocity measured by the floats to absolute horizontal velocity (Phillips and Bindoff 2014).

The Argo delayed-mode quality control is a rigorous and internationally standardized procedure to ensure that the temperature and salinity profiles are free of detectable errors and biases (Wong et al. 2013). The CSIRO software was adapted to fit the sampling strategy and data format of the EM-APEX floats, which are different than that of the Argo profiling floats. The procedure includes identifying bad pressure points, checking for density inversions, testing for surface pressure drifts, checking for salinity drifts, and applying a thermal lag correction. The thermal lag correction is tailored for the EM-APEX floats following the method of Johnson et al. (2007), and values for the correction parameters are $\alpha = 0.023$ and $\tau = 25.0$ s. The quality control of the EM-APEX float velocity data is described in more detail in Phillips and Bindoff (2014).

b. Regional oceanography

The profiles from the EM-APEX profiling floats stretch over 6500 km of float trajectories in the vicinity

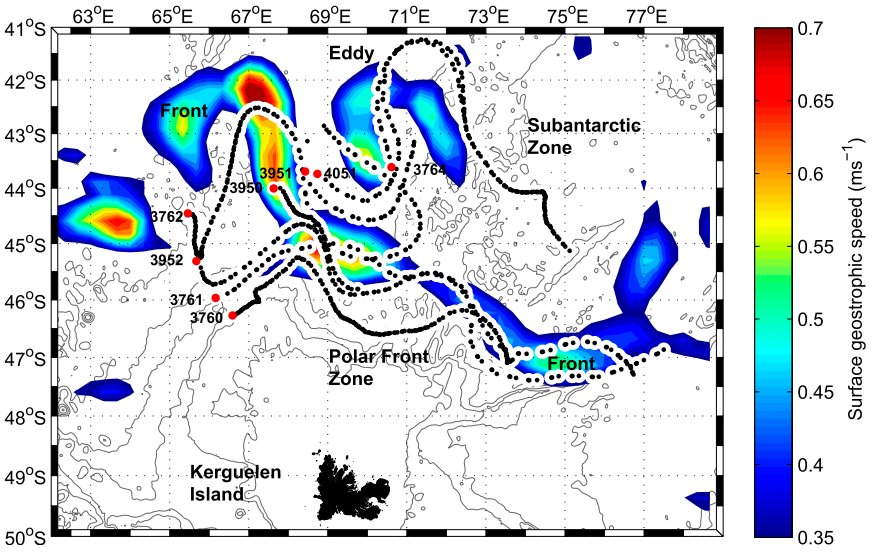

FIG. 1. Trajectories of EM-APEX floats overlying topographic contours (gray) ranging from 500 to 5000 m at 800-m increments. Each black dot denotes the surface location of a float profile. Float numbers are indicated next to their deployment locations (red dots). To identify frontal jets, mean surface geostrophic speed over 0.35 m s^{-1} is shown for the deployment period (color scale). The "front" label indicates the presence of the Subantarctic/Subtropical Front (SAF/STF region).

of the Kerguelen Plateau (41°–50°S, 61°–79°E), sampling the upper water column (0–1600 m) between November 2008 and January 2009 (Fig. 1). The EM-APEX float profiles of potential temperature, salinity, horizontal velocity, and buoyancy frequency help us identify oceanographic features near the Kerguelen Plateau (Fig. 2). Profiles are shown in sampling order and are grouped by floats, and floats are organized by decreasing mean sampling latitude. This gives the composite trajectories the appearance of a meridional transect, with the southernmost float on the left (Fig. 2).

Fronts can be identified using hydrographic criteria such as velocity maxima location, water-mass distribution, and locations where certain hydrographic properties cross particular depths (Belkin and Gordon 1996). Using surface velocity maxima determined from satGEM (Meijers et al. 2011), a weekly geostrophic velocity product, Meyer et al. (2015) found a coherent and intense jet north of the Kerguelen Plateau over the sampling period of the EM-APEX floats (18 November 2008 to 30 January 2009). The jet was identified as the middle and northern branches of the Subantarctic Front, likely merged with the southern branch of the Subtropical Front. We refer to this Subantarctic/Subtropical Front as the SAF/STF region (Figs. 1, 2). Another feature identified by Meyer et al. (2015) from the EM-APEX data and the satGEM product is a large meander-like structure pinching off the SAF/STF region, hereinafter referred to as the eddy. The eddy is located between 44° and 42°S and 69° and 73°E (Fig. 1). The EM-APEX floats do not sample the Polar Front (Meyer et al. 2015).

We sort the EM-APEX float profiles according to their position relative to the SAF/STF region. They are either in the region north of the SAF/STF region (Subantarctic Zone), in the SAF/STF region, in the region south of the SAF/STF region (Polar Front Zone), or in the eddy. Profiles that are located in a region of geostrophic flow velocity larger than 0.35 m s^{-1} are considered to be in the SAF/STF region, or in the eddy if not along the main axis of the SAF/STF region. The rest of the profiles are assigned to either the Subantarctic Zone or to the Polar Front zone. Half the profiles are found to be in the Polar Front Zone, 23% in the SAF/STF region, 10% in the Subantarctic Zone, and 17% in the eddy.

The characteristics of the oceanographic fronts in the area and eddy observed in this dataset are described in more detail in Meyer et al. (2015) (section 4a).

3. Linear wave theory

a. Governing equations

The momentum equations of a continuously stratified, incompressible, homogeneous fluid on the f plane with density ρ and subject to small perturbations about the background state of rest are

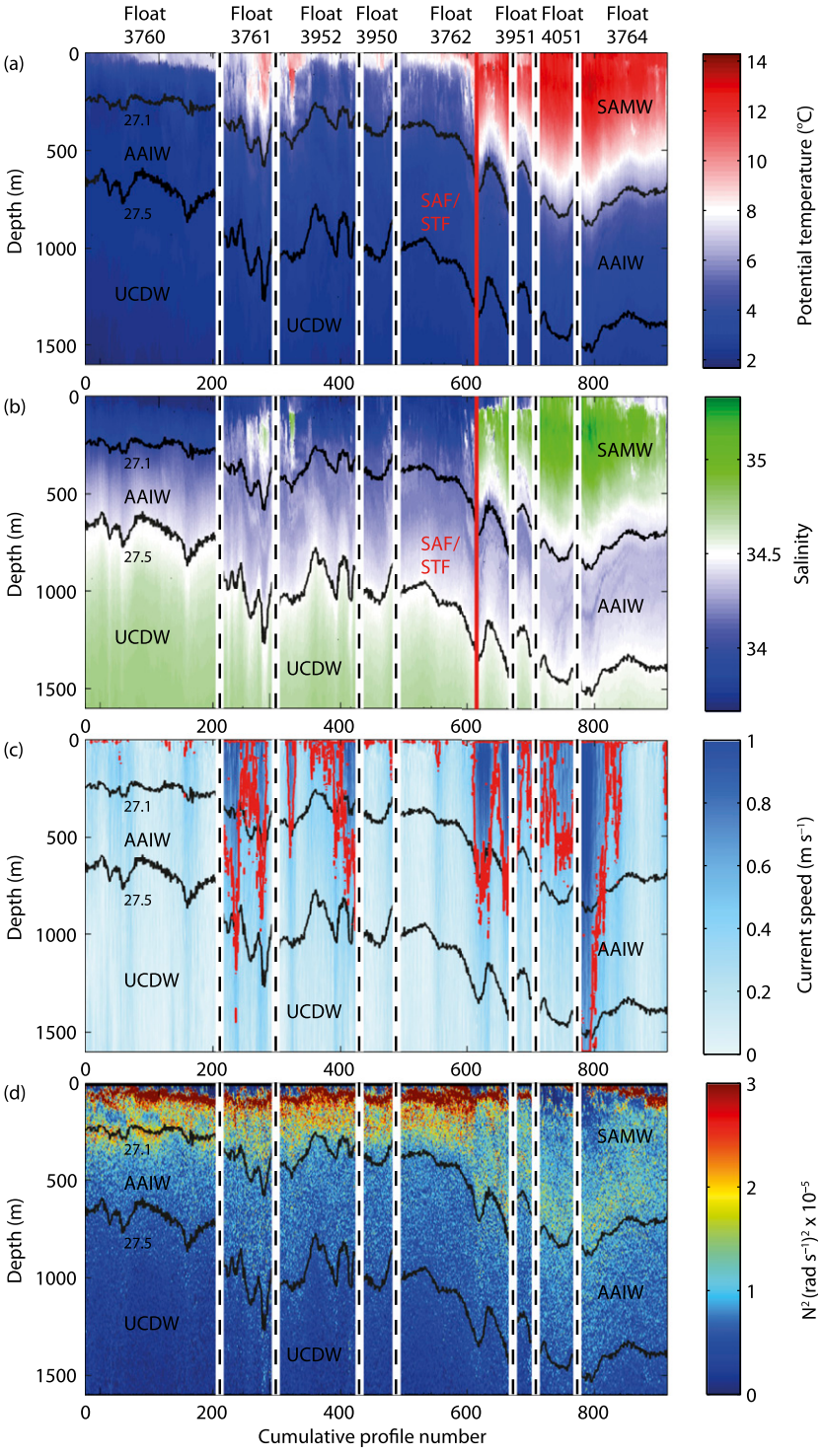

FIG. 2. Vertical distribution of (a) potential temperature, (b) salinity, (c) current speed, and (d) buoyancy frequency squared (N^2) along the trajectories of the eight EM-APEX floats. The position of the SAF/STF region is indicated by the vertical red line in (a) and (b). Selected labeled potential density (σ_θ) contours delimit water masses north and south of the SAF/STF region: Subantarctic Mode Water (SAMW) is defined as $\sigma_\theta \leq 27.1\,\mathrm{kg\,m^{-3}}$, Antarctic Intermediate Water (AAIW) is defined as $27.1 \leq \sigma_\theta \leq 27.5\,\mathrm{kg\,m^{-3}}$, and Upper Circumpolar Deep Water (UCDW) is defined as $\sigma_\theta \geq 27.5\,\mathrm{kg\,m^{-3}}$. The $0.55\,\mathrm{m\,s^{-1}}$ current speed contour (red) identifies the location of jets in (c). The vertical dashed lines separate floats.

$$\frac{\partial u}{\partial t} - fv = -\frac{1}{\rho_0}\frac{\partial p}{\partial x}, \tag{1}$$

$$\frac{\partial v}{\partial t} + fu = -\frac{1}{\rho_0}\frac{\partial p}{\partial y}, \tag{2}$$

$$\frac{\partial w}{\partial t} = -\frac{1}{\rho_0}\frac{\partial p}{\partial z} + b, \tag{3}$$

$$\frac{\partial u}{\partial x} + \frac{\partial v}{\partial y} + \frac{\partial w}{\partial z} = 0, \quad \text{and} \tag{4}$$

$$\frac{\partial \rho}{\partial t} + w\frac{\partial \overline{\rho}}{\partial z} = 0, \tag{5}$$

where (u, v, w) are the (x, y, z) components of the velocity, p is the pressure, $b = -g\rho/\rho_0$ is the buoyancy, the overbar indicates the mean state, f is the Coriolis frequency, and ρ is the density defined as

$$\rho = \rho_0 + \overline{\rho}(z) + \rho'(x, y, z, t), \tag{6}$$

where ρ_0 is the reference density.

b. Dispersion relation

The direction of propagation of a plane wave phase is given by the three-dimensional wave vector $\mathbf{p} = (k, l, m)$, where m is the vertical plane component, also called the vertical wavenumber, and where k and l combine as the horizontal wave vector $\mathbf{k} = (k, l)$ (Fig. 3). The azimuth φ of the horizontal wave vector is $\varphi = \tan^{-1}(l/k)$, and the magnitude of the horizontal wave vector is the horizontal wavenumber $k_h = |\mathbf{k}| = (k^2 + l^2)^{1/2}$ (Fig. 3).

To obtain the dispersion relation, we assume that the background stratification is constant (Phillips 1977). The internal wave variables can then be written in the form of plane wave solutions

$$w = w_0 e^{\pm i(kx+ly+mz-\omega t)} = w_0 e^{\pm i(\mathbf{p}\cdot\mathbf{r}-\omega t)}, \tag{7}$$

where ω is the observed frequency, often referred to as the Eulerian frequency, measured by a stationary observer and the position vector $r = (x,y,z)$. The intrinsic frequency ω_0 is measured by an observer moving with the mean flow:

$$\omega_0 = \omega - \mathbf{k}\cdot\overline{\mathbf{U}}. \tag{8}$$

In the absence of a mean flow, both frequencies are equal.

In the linearized momentum equations [Eqs. (1)–(5)], the independent variables, which are the vorticity and pressure terms, can be eliminated to obtain the internal wave equation in vertical velocity w (Gill 1982):

$$\frac{\partial^2}{\partial t^2}\left(\nabla_h^2 w + \frac{\partial^2 w}{\partial z^2}\right) + f^2\frac{\partial^2 w}{\partial z^2} + \nabla_h^2 w N^2 = 0, \tag{9}$$

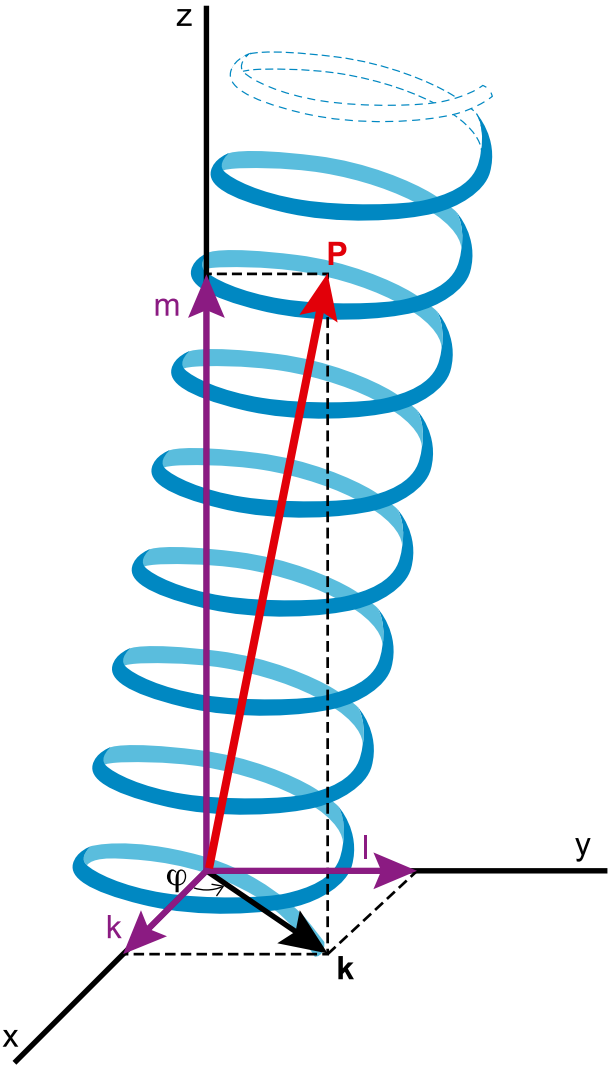

FIG. 3. Coordinate system used to describe internal waves. The wave vector is $\mathbf{p} = (k, l, m)$ while the horizontal wave vector is $\mathbf{k} = (k, l)$ in the direction of increasing (x, y, z). The horizontal azimuth φ of the horizontal wave vector determines the orientation of the wave vector $\mathbf{p}$ in the horizontal plane.

where $\nabla_h^2 = \partial^2/\partial x^2 + \partial^2/\partial y^2$ is the horizontal Laplacian operator and N is the buoyancy frequency.

Substituting the plane wave solution [Eq. (7)] into the internal wave equation [Eq. (9)] yields the dispersion relation

$$\frac{k_h^2}{m^2} = \frac{f^2 - \omega_0^2}{\omega_0^2 - N^2}. \tag{10}$$

c. Polarization relations

Assuming a constant stratification and plane wave solutions where the variables are proportional to $e^{i(\mathbf{p}\cdot\mathbf{r}-\omega t)}$, the dependent variables can be expressed in

terms of wave amplitude [see Polzin and Lvov (2011) for equations]. These polarization relations lead to three diagnostics.

1) The first diagnostic provides an estimate of the ratio of horizontal kinetic energy E_k to potential energy E_p for a single internal wave:

$$\frac{E_k}{E_p} = \frac{\omega_0^2 + f^2}{\omega_0^2 - f^2}. \tag{11}$$

2) The second diagnostic provides an estimate of the ratio of velocity variance in the clockwise (E_{CW}) and counterclockwise (E_{CCW}) rotating components (rotary ratio). The velocity vector **u** draws an elliptical helix with depth (Fig. 3) due to the rotation for the earth. In this near-inertial rotation of the velocity vector, the ratio of velocity variance in the E_{CW} and in the E_{CCW} rotating component is

$$\frac{E_{\mathrm{CW}}}{E_{\mathrm{CCW}}} = \frac{(\omega_0 + f)^2}{(\omega_0 - f)^2}, \tag{12}$$

where the convention is that a positive intrinsic frequency implies downward phase (and therefore upward energy) propagation of the internal wave and corresponds to the dominant CW rotation of the velocity vector in the Southern Hemisphere (Polzin and Lvov 2011).

3) The third diagnostic provides an estimate of the azimuth of the horizontal wave vector **k** from the rotary-buoyancy coherence. Using the linear polarization relations for a single plane wave and near-inertial interpretations of clockwise (CW = $u - iv$) and counter clockwise (CCW = $u + iv$) phase rotation with depth, the observed clockwise-buoyancy phase is

$$\tan(\phi) = \tan[\widehat{\mathrm{CW}}\hat{b}^*/(\widehat{\mathrm{CW}}\widehat{\mathrm{CW}}^*)^{1/2}(\hat{b}\hat{b}^*)^{1/2}] = \frac{-k}{-l}, \tag{13}$$

and the counterclockwise-buoyancy phase is

$$\tan(\phi) = \tan[\widehat{\mathrm{CCW}}\hat{b}^*/(\widehat{\mathrm{CCW}}\widehat{\mathrm{CCW}}^*)^{1/2}(\hat{b}\hat{b}^*)^{1/2}] = \frac{k}{-l}, \tag{14}$$

where $\hat{}$ represents the Fourier transform, * represents the complex conjugate, Eq. (13) assumes a single wave of downward phase (upward energy propagation), and Eq. (14) assumes a single wave having upward phase (downward energy propagation). The observed phase ϕ of the rotary velocity component can be interpreted as the horizontal azimuth φ of the horizontal wave vector in polar coordinates as

$$\varphi = \tan^{-1}\left[\frac{-\cos(\phi)}{\sin(\phi)}\right] \tag{15}$$

for waves with a velocity vector rotating CCW and as

$$\varphi = \tan^{-1}\left[\frac{-\cos(\phi)}{-\sin(\phi)}\right] \tag{16}$$

for waves with a velocity vector rotating CW. See appendix A for derivations.

d. Properties of internal waves

By rearranging the dispersion relation [Eq. (10)], we obtain an equation for the vertical wavenumber m:

$$m = \pm k_h \left(\frac{N^2 - \omega_0^2}{\omega_0^2 - f^2}\right)^{1/2}. \tag{17}$$

Equation (17) implies that for $\omega_0 > f$, we have $m > 0$. Consequently, if the intrinsic frequency of the internal wave ω_0 is larger than the modulus of the intrinsic frequency relative to $|f|$, the horizontal velocity vector is rotating in a counterclockwise manner in the Southern Hemisphere.

The group velocity $\mathbf{C}_g$ is the gradient of the intrinsic frequency in the vertical wavenumber space:

$$\mathbf{C}_g = \left(\frac{\partial\omega_0}{\partial k}, \frac{\partial\omega_0}{\partial l}, \frac{\partial\omega_0}{\partial m}\right), \quad \text{and} \tag{18}$$

$$\mathbf{C}_g = \left[\frac{k(N^2 - \omega_0^2)^2}{\omega_0 m^2 (N^2 - f^2)}, \frac{l(N^2 - \omega_0^2)^2}{\omega_0 m^2 (N^2 - f^2)}, -\frac{(\omega_0^2 - f^2)(N^2 - \omega_0^2)}{\omega_0 m (N^2 - f^2)}\right], \tag{19}$$

which we can reformulate (see appendix B for details). Using the hydrostatic approximation ($\omega_0^2 \ll N^2$) as

$$\mathbf{C}_g \simeq \left(\frac{kN^2}{\omega_0 m^2}, \frac{lN^2}{\omega_0 m^2}\right), \tag{20}$$

the magnitude C_{gh} of the vector $\mathbf{C}_g$ is therefore

$$C_{gh} = \sqrt{\left(\frac{kN^2}{\omega_0 m^2}\right)^2 + \left(\frac{lN^2}{\omega_0 m^2}\right)^2}. \tag{21}$$

The parameters and diagnostics described in this section are summarized in Table 1.

TABLE 1. Internal wave parameters and relations based on single plane wave solutions of the form $e^{i(kx+ly+mz-\omega t)}$ to the linearized equations of motion.

Name	Definition	Units
Local Coriolis frequency	$f = 1 \times 10^{-4}$	s^{-1}
Intrinsic frequency	$\omega_0 = \omega - \mathbf{k} \cdot \overline{\mathbf{U}}$	s^{-1}
Wave vector	$\mathbf{p} = (k, l, m)$	
Horizontal wavenumber	$k_h = (k^2 + l^2)^{1/2}$	cpm
Dispersion relation	$k_h^2/m^2 = (f^2 - \omega_0^2)/(\omega_0^2 - N^2)$	
Energy ratio	$E_k/E_p = (\omega_0^2 + f^2)/(\omega_0^2 - f^2)$	
Rotary ratio	$E_{CW}/E_{CCW} = (\omega_0 + f)^2/(\omega_0 - f)^2$	
Vertical wavenumber	$m = \pm k_h[(N^2 - \omega_0^2)/(\omega_0^2 - f^2)]^{1/2}$	cpm
Group velocity	$C_{gh} = \{[(kN^2)/(\omega_0 m^2)]^2 + [(lN^2)/(\omega_0 m^2)]^2\}^{1/2}$	$m\,s^{-1}$

4. Method of analyzing internal waves

Identifying internal waves and extracting their properties from observations is challenging. In this section, we explain how we obtain the properties of 46 internal waves in the region of the Kerguelen Plateau, applying linear wave theory to coherent features identified in vertical profiles of horizontal velocity. We first identify coherent features in real space; next, we interpolate variables onto a Wentzel–Kramers–Brillouin (WKB) coordinate and then execute a spectral analysis in the WKB stretched coordinate (see appendix C for details). Doing so, we make the assumption that observed coherent features are internal waves, as previously done (Polzin 2008; Müller et al. 1978). This analysis is restricted to depths at which the theory can be applied and where velocity observations are available (200–1600 m). We demonstrate the method by presenting the analysis of one of the 46 internal waves identified as internal wave 5. We define internal wave 5 as the coherent feature that ranges from approximately profile 64 to profile 76 between 600 and 1000 m in float 3761 velocity data (Fig. 4c). This wave has a very clear signal in the velocity anomaly profiles and a corresponding large peak in the energy spectrum. As a result, internal wave 5 makes a great case example. The method described below was also applied to the other 45 internal waves identified.

a. *Estimating the buoyancy frequency and buoyancy perturbation*

The buoyancy frequency N is expressed as an angular frequency in radians per second

$$N = \sqrt{gE} \simeq \sqrt{-\frac{g}{\rho_\theta}\frac{d\rho_\theta}{dz}}, \tag{22}$$

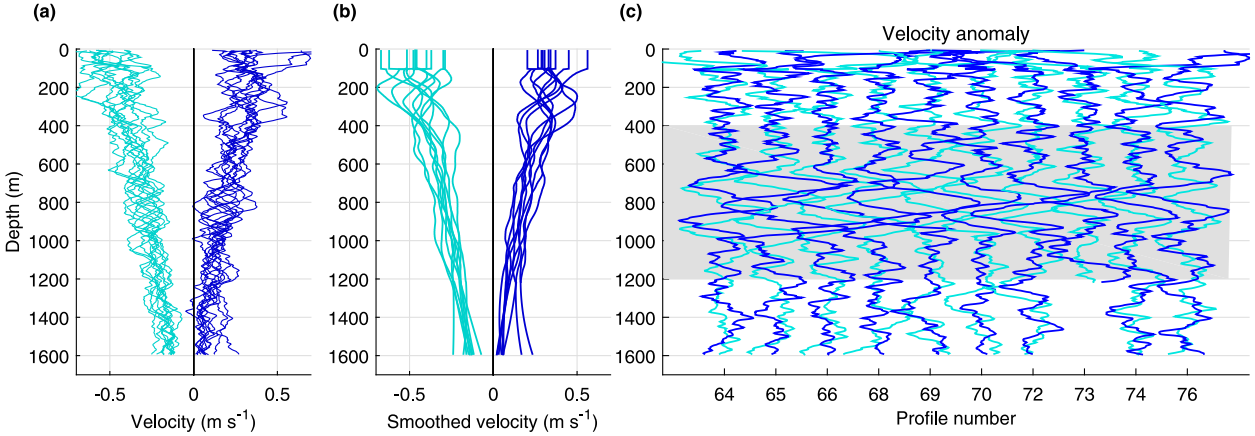

FIG. 4. (a) Float 3761 eastward horizontal velocity (dark blue) and northward horizontal velocity (cyan) from profiles 64–76. (b) Corresponding smoothed velocity profiles where the smoothed velocity is the result of a sliding second-order polynomial regression with an increasing vertical fit window length. (c) Time series of corresponding horizontal velocity anomaly. The velocity anomaly profile is defined as the horizontal velocity minus the smoothed velocity. Internal wave 5 is identified by the coherence in the velocity anomaly between approximately 400 and 1200 m depth (gray shading). Missing profile numbers correspond to profiles interrupted by a drift at constant depth that were excluded from this analysis.

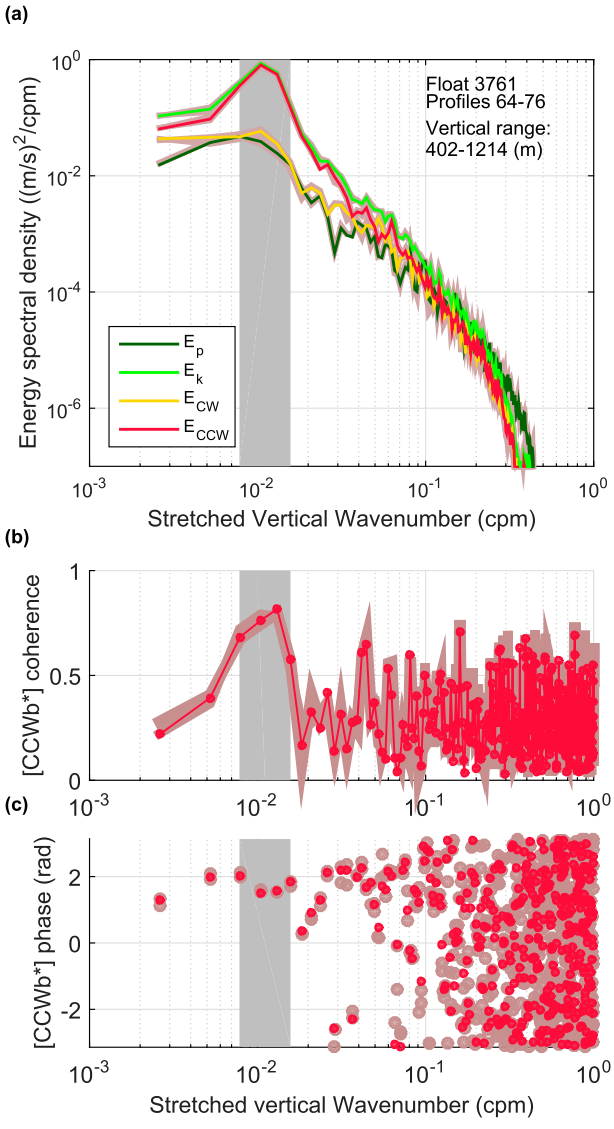

FIG. 5. (a) Horizontal potential (E_p) and kinetic (E_k) energy as well as CW (E_{CW}) and CCW (E_{CCW}) rotary spectra in terms of stretched vertical wavenumber of horizontal velocity profiles 64–76 (float 3761) computed using data between 402 and 1126 m. Internal wave 5 is identified by the peak in both kinetic and downward (CCW) energy at vertical wavenumber $\sim 1 \times 10^{-2}$ cpm (gray shading). (b) Rotary-buoyancy coherence (CCWb*) and (c) phase (CCWb*) estimates for internal wave 5 (profiles 64–76, float 3761). Internal wave 5 peak in the energy spectra, coherence, and corresponding phase points are shaded in gray. The standard deviation for each point of the energy spectra, the rotary-buoyancy coherence, and the rotary-buoyancy phase are also shaded in gray for each point.

where g is the acceleration due to gravity, E is the stability of the water column, and ρ_θ is the potential density referenced to the midpoint pressure, following the adiabatic levelling method (McDougall and Barker 2014). We estimate two buoyancy frequencies that are derived over different time, horizontal, and vertical length scales: a small-scale squared buoyancy frequency N^2 and a mean squared buoyancy frequency $\langle N^2_{\text{ref}} \rangle$. The latter is derived applying a time average denoted by $\langle\,\rangle$ brackets. See Meyer et al. (2015) for full details.

We decompose the observed buoyancy b into a mean buoyancy $\overline{b}$ and a small-amplitude internal wave buoyancy perturbation b' such that $b = \overline{b} + b'$. The observed buoyancy b is derived from N^2, while the mean or reference buoyancy $\overline{b}$ is derived from $\langle N^2_{\text{ref}} \rangle$.

b. Identifying internal waves from coherent features

The time–depth series of the velocity profiles show the presence of many internal waves. Altogether, internal waves are found in 400 profiles out of 914 velocity profiles available. To locate internal waves, we first visually identify regions of coherence in the horizontal velocity profiles. Such a region is highlighted in gray on Fig. 4c. Next, we compute the energy density and rotary spectra of the selected velocity profiles as well as the rotary-buoyancy coherence and rotary-buoyancy phase plots (Fig. 5). If the energy spectra and the rotary-buoyancy coherence have peaks at the same wavenumber and the coherence is statistically significant, we proceed to analyze that group of velocity profiles to extract internal wave properties.

Demodulation methods to identify wave packets in velocity datasets have been applied in previous studies (Cuypers et al. 2013). The time resolution of the velocity dataset in this study puts fundamental limits on our ability to apply such methods. To estimate the error associated with the initial choice of velocity profiles on the derived internal wave properties and the sensitivity of internal wave properties to the spectral coherence, we apply a bootstrap-like method to a subset of six internal waves. For a given wave, we compute its vertical wavenumber and energy spectra several times, withholding a different single velocity profile from the analysis each time. If a wave is made up of 10 horizontal velocity profiles, we compute the spectra 10 times, each time withholding a different velocity profile. We then compare the estimated internal wave properties from each run. From the range of obtained values, we compute the standard deviation σ (Table 2, values in bold). This method shows that the vertical wavenumber estimates are very robust and that the E_k/E_p energy ratio estimates are also robust.

The eastward and northward horizontal velocity anomaly profiles are defined as the horizontal velocity profiles (eastward and northward) subtracted from the smoothed velocity profiles (eastward and northward),

TABLE 2. Properties of analyzed internal waves from the EM-APEX dataset: number of the internal wave, float number, profiles in which the coherent feature was identified, spectral peak and energy propagation, E_k/E_p energy ratio, depth of wave, vertical wavelength λ, horizontal wavelength λ_h, vertical wavenumber m, horizontal azimuth ϕ, Doppler shift (Dshift), horizontal group velocity C_{gh}, period T, dissipation time scale τ_ε, and propagation time scale τ_{prop}. For internal wavenumbers 5, 10, 15, 30, 36, and 47, the standard deviation of the derived property is indicated in bold.

Wave	Float	Profiles	Peak	E_k/E_p	Depth (m)	λ (m)	λ_h (km)	m (cpm)	ϕ (°)	Dshift $\times 10^{-3}$ (rad s^{-1})	C_{gh} (cm s^{-1})	T (h)	τ_ε (days)	τ_{prop} (days)
5	3761	64–76	E_k down	22.2	800	206	15.0	0.01	7	0.07	2.4	15.8	8	7
				2.7		**0.65**	**0.95**	**1.1×10^{-5}**	**7.1**	**0.0068**	**0.12**	**0.075**	**1.2**	**0.4**
6	3761	80–84	E_k up	4.57	350	162	4.4	0.01	42	−0.40	3.3	13.1	20	5
7	3761	105–114	E_k down	34.8	400	321	31.9	0.006	−92	0.03	3.1	15.9	16	6
8	4051	5–10	E_k	24.8	700	188	19.8	0.009	114	−0.12	2.6	16.6	4	7
9	4051	29–48	E_k down	14.7	900	214	14.7	0.009	47	0.08	3.2	16.2	30	5
10	4051	46–53	E_k up	3.91	300	255	8.9	0.007	134	−0.2	7.3	13.7	9	2
				0.4		**4.4**	**0.69**	**2.4×10^{-5}**	**16**	**0.065**	**0.34**	**0.46**	**1.3**	**0.1**
11	4051	54–64	E_k down	11.02	500	161	11.2	0.01	70	0.28	3.1	16.5	5	6
12	4051	73–86	E_k down	23.2	600	182	19.2	0.009	14	0.001	2.6	17.2	10	7
13	4051	64–78	E_k down	43.5	600	90.3	13.3	0.02	22	0.12	0.9	17.7	5	18
15	3951	40–46	E_k up	38.5	500	97.1	12.9	0.02	−27	0.04	1.1	16.9	17	16
				6.9		**0.56**	**1.15**	**2.9×10^{-5}**	**22**	**0.037**	**0.08**	**0.078**	**4**	**1.3**
16	3951	34–40	E_k down	49.2	300	196	30.9	0.008	−43	0.09	2.0	16.9	68	9
17	3951	4–11	E_k down	13.4	400	64.8	5.2	0.025	−54	0.74	1.3	16.0	9	14
18	3950	4–20	E_k down	13.8	800	198	11.9	0.011	−119	0.05	2.8	16.0	80	6
19	3950	20–24	E_k down	8.94	800	258	12.4	0.008	−156	0.002	4.5	15.3	14	4
20	3950	25–30	E_k up	9.02	1000	227	11.3	0.009	−152	0.031	4.1	15.3	16	4
21	3950	30–37	E_k up	14.4	1000	138	7.8	0.017	−102	−0.02	1.8	15.9	10	10
22	3950	49–54	E_k up	20.3	1000	313	21.6	0.007	−38	−0.03	3.5	16.2	8	5
23	3950	66–77	E_k up	16.8	700	218	14.4	0.010	23	−0.06	2.8	15.8	20	6
24	3764	5–14	E_k down	72.0	400	78.3	13.5	0.023	−171	0.003	0.6	17.2	1	29
25	3764	14–22	E_k up	24.0	800	193	19.2	0.009	10	−0.07	2.5	17.0	11	7
26	3764	22–33	E_k down	20.7	700	192	19.3	0.009	−144	−0.10	2.9	17.1	10	6
27	3764	52–80	E_k down	23.4	600	123	13.1	0.014	128	−0.06	1.7	17.1	1	10
28	3764	65–70	E_k down	38.9	400	163	19.9	0.012	126	−0.03	1.6	17.2	20	11
29	3764	112–122	E_k down	15.9	600	118	9.5	0.015	138	−0.05	1.9	16.2	1	9
30	3764	148–154	E_k down	73.7	700	136	21.3	0.015	141	0.0002	0.9	16.9	10	19
				20		**0.56**	**3.0**	**4.0×10^{-5}**	**21**	**0.0039**	**0.16**	**0.084**	**2.6**	**2.6**
31	3952	74–81	E_k up	9.57	500	338	18.0	0.006	13	−0.05	6.3	15.1	3	3
32	3952	84–93	E_k up	24.6	1000	181	11.6	0.015	−57	−0.03	1.6	16.0	1	11
33	3952	102–110	E_k up	18.1	1000	122	7.4	0.020	40	−0.17	1.3	15.8	1	13
34	3952	134–138	E_k up	87.1	900	180	24.8	0.013	−54	−0.09	1.0	16.2	13	18
35	3952	146–150	E_k up	34.8	600	141	14.0	0.014	153	0.20	1.4	15.8	18	13
36	3952	160–166	E_k down	7.13	600	359	14.7	0.006	−28	0.18	7.1	14.1	53	2
				0.7		**50**	**2.4**	**57×10^{-5}**	**8**	**0.016**	**0.94**	**0.20**	**7.7**	**0.2**
37	3952	169–174	E_k down	15.2	700	200	12.3	0.011	6	0.22	2.8	15.3	109	6
38	3760	87–94	E_k down	15.6	700	255	16.2	0.008	−16	0.08	3.4	15.8	32	5

TABLE 2. (*Continued*)

Wave	Float	Profiles	Peak	E_k/E_p	Depth (m)	λ (m)	λ_h (km)	m (cpm)	ϕ (°)	Dshift $\times 10^{-3}$ (rad s^{-1})	C_{gh} (cm s^{-1})	T (h)	τ_ε (days)	τ_{prop} (days)
39	3760	95–99	E_k down	58.4	900	198	20.6	0.013	−77	0.06	1.2	16.4	118	15
40	3760	116–126	E_k up	14.5	800	226	12.2	0.011	−24	−0.06	2.8	15.5	81	6
41	3760	186–191	E_k up	12.9	800	298	15.2	0.008	−15	−0.03	4.0	15.2	12	4
42	3760	204–210	E_k up	17.6	1100	173	8.4	0.017	−44	−0.03	1.6	15.6	87	11
43	3760	234–239	E_k up	37.9	600	135	13.9	0.015	41	0.04	1.2	16.0	34	14
44	3762	4–21	E_k up	11.9	600	165	9.5	0.012	−30	−0.04	2.6	15.7	21	7
45	3762	85–90	E_k down	7.27	900	329	13.4	0.007	38	0.12	6.0	14.8	24	3
46	3762	176–180	E_k down	16.7	900	208	14.6	0.010	−41	0.18	2.8	16.2	31	6
47	3762	190–194	E_k down	12.4	600	171	11.3	0.012	−122	−0.28	3.0	15.5	80	6
				3.9		**3.1**	**1.9**	**7.9×10^{-5}**	**16**	**0.086**	**0.38**	**0.34**	**23**	**0.8**
48	3762	208–210	E_k down	8.77	600	159	52.7	0.012	144	−4.31	20	2.4	47	1
49	3762	216–220	E_k down	10.8	500	216	14.1	0.008	−25	−0.21	4.3	15.6	25	4
50	3762	240–244	E_k down	63.1	300	131	20.2	0.014	58	0.04	1.0	17.3	212	17

where the smoothed velocity profiles are the result of a sliding second-order polynomial regression with an increasing vertical fit window length (Fig. 4). These velocity anomaly profiles provide information about the location of internal waves and about their phase propagation.

The coherent features used to define internal waves in the EM-APEX data might be partially biased toward internal waves with lower frequencies and large horizontal scales. This is the result of using coherence in the amplitude of the observations to identify internal waves. Higher frequency internal waves have smaller amplitude and are therefore harder to identify with the method applied. Analyzing data resolving the full water column would increase the confidence of statistics, in particular for the upward propagating internal waves generated in deeper waters.

c. *Wavelength, frequency, and period*

Next we consider the vertical wavenumber and energy density spectra for the profiles in which internal wave 5 is identified (Fig. 5a). The equation $E = E_k + E_p$ is the energy density composed of a kinetic (E_k) and a potential (E_p) component. We find a peak in kinetic energy ($E_k > E_p$) with a vertical wavenumber $m = 0.0049$ cpm, which is matched by a peak in CCW rotary motions ($E_{\text{CCW}} > E_{\text{CW}}$; Fig. 5a, gray shading). These peaks are identified as the spectral signature of internal wave 5. The CCW rotary peak in the spectra confirms the earlier finding of upward phase propagation. Note that in stretched coordinates $m = 0.01$ cpm (Fig. 5a).

From the vertical wavenumber m of internal wave 5, we estimate its vertical wavelength $\lambda = 206$ m. We also estimate the intrinsic frequency ω_0 of internal wave 5 by rearranging the energy ratio equation: $\omega_0 = f[(E_p + E_k)/(E_k - E_p)]^{1/2} = 1.1 \times 10^{-4}$ rad s^{-1} (Table 1), where we use observed energy estimates from the spectra. Subsequently, we estimate the period $T = 2\pi/\omega_0 = 5.7 \times 10^4$ s $= 15.8$ h of internal wave 5.

d. *Horizontal wavenumber*

The horizontal wavenumber k_h of internal wave 5 can be estimated using the dispersion relation (Table 1) where the hydrostatic approximation ($\omega_0^2 \ll N^2$) has been applied such that $k_h = \pm m/N(\omega_0^2 - f^2)^{1/2} = 4.2 \times 10^{-4}$ rad m^{-1}. Here we use $N = N_0 = 0.005\,24$ s^{-1} $= 3$ cph to match the WKB stretched coordinates. We then estimate the horizontal wavelength of internal wave 5: $\lambda_h = 2\pi/k_h = 1.5 \times 10^4$ m $= 15$ km.

Given the rotary-buoyancy coherence, we estimate the horizontal wavenumber bias associated to background noise in potential energy for a subset of six internal waves (Polzin 2008). We find that this bias

translates in the horizontal wavenumber being overestimated by a mean factor of 0.62 for this subset.

e. Horizontal wave vector azimuth and horizontal group velocity

From the spectral coherence, we can examine the relation between the rotary, either CCW or CW, and buoyancy perturbation b'. The analysis of the coherence between the rotary (CCW in this case) and the buoyancy perturbations shows a peak in the rotary-buoyancy coherence that matches the peak in the energy spectrum at approximately 0.01 cpm (Fig. 5b). The peak in the rotary-buoyancy coherence corresponds to a mean phase $\phi = 1.7$ rad (Fig. 5c). From this peak, we estimate the horizontal wave vector $\mathbf{k}$ components (k, l), where $k = k_h \sin(\phi) = 4 \times 10^{-4}$ rad and $l = -k_h \cos(\phi) = 5 \times 10^{-5}$ rad (for CCW rotation).[1]

For a subset of six internal waves, we derive the uncertainty in the mean phase estimate ϕ given the rotary-buoyancy coherence (Table 2, bold values in ϕ column). The standard deviation of the phase for internal wave 5 is $\sigma_5 = \pm 0.1$, and the mean standard deviation over the subset is $\sigma_{\text{mean}} = \pm 0.25$.

The horizontal azimuth φ of the horizontal wave vector $\mathbf{k}$ of internal wave 5 is estimated with the observed phase ϕ: $\varphi = \tan^{-1}[-\cos(\phi)/\sin(\phi)] = 7.2°$, where $\phi = 1.7 \pm 0.1$ rad [see third diagnostic in polarization relations: Eqs. (13)–(16)]. The horizontal azimuth indicates that internal wave 5 is propagating westward. The horizontal intrinsic group velocity C_{gh} of internal wave 5 is estimated, using the k and l vectors derived above: $C_{gh} = 0.024\,\text{m s}^{-1}$ (Table 1). We set $N = N_0 = 0.005\,24\,\text{s}^{-1}$ to account for WKB stretched coordinates.

f. Wave–mean interactions

We can estimate properties of the internal waves with regards to the flow field, such as the Doppler shift associated with advection by the mean flow and wave–mean interaction time scales.

The Doppler shift is defined as $\mathbf{k} \cdot \overline{\mathbf{U}} = k\overline{u} + l\overline{v}$, where $\overline{u}$ and $\overline{v}$ are the mean absolute velocity estimates for the selected profiles within a depth range: $(\overline{u}, \overline{v}) = (0.2, -0.3)\,\text{m s}^{-1}$. The depth range, based on visual inspection of the selected velocity profiles, covers a minimum of 600 m and is centered on the identified internal wave velocity coherence signal. A positive Doppler shift is against the flow and a negative Doppler shift is with the flow field. In the case of internal wave 5, the Doppler shift, $\mathbf{k} \cdot \mathbf{u} = 6.8 \times 10^{-5}\,\text{rad s}^{-1}$, is similar to the local inertial frequency $|f| = 1.05 \times 10^{-4}\,\text{rad s}^{-1}$. Confidence in Doppler shift estimates depends on the accuracy of the horizontal wave vector azimuth and therefore the rotary phase estimate.

We consider a dissipation time scale τ_ε:

$$\tau_\varepsilon = \frac{2E}{\varepsilon_{\text{GM}}} \left(\frac{\lambda_{c\text{GM}}}{\lambda_c} \right)^2, \tag{23}$$

where $E = \int_{0.005}^{0.018} (E_P + E_K)\, dm = 0.0011\,\text{m}^2\,\text{s}^{-2}$ is the total energy contained in the peak associated with internal wave 5 on the energy spectrum, $\varepsilon_{\text{GM}} = 8 \times 10^{-10}\,\text{W kg}^{-1}$ is the GM76 reference dissipation rate, $\lambda_{c\text{GM}} = 10$ m is the GM76 reference critical wavenumber, and $\lambda_c = 20$ m is the observed critical wavenumber for internal wave 5. Here GM refers to Garrett and Munk (1972) who were the first to describe and model the background internal wave field. Additional work on this model by Cairns and Williams (1976) is denoted GM76. The observed critical wavenumber is defined as $\lambda_c = 1/m_c$. The cutoff vertical wavenumber m_c is the threshold where there is a transition from quasi-linear wave–wave interactions to strongly nonlinear wave breaking (D'Asaro and Lien 2000; Polzin et al. 2014). Here, the high vertical resolution of the velocity data from the EM-APEX floats (~3 m) enables us to resolve m_c for each profile. We define m_c as the point where the integrated shear variance reaches $2\pi N^2/10$ [see Eq. (20) in Polzin et al. 2014] and derive it for each vertical segment. Its mean value is 1/16 cpm, that is, the mean observed critical wavenumber is $\lambda_c = 16$ m. Inputting all variables into Eq. (23), we find $\tau_\varepsilon = 7.0 \times 10^5$ s = 8 days for internal wave 5.

We also consider a propagation time scale τ_{prop} that estimates the time it would take for the internal wave to propagate away from the flow field:

$$\tau_{\text{prop}} = \frac{L_{\text{Ro}}}{C_{gh}}, \tag{24}$$

where C_{gh} is the horizontal intrinsic group velocity of internal wave 5 and we set the local first baroclinic Rossby radius of deformation to $L_{\text{Ro}} = 15\,000$ m (Chelton et al. 1998). The propagation time scale for internal wave 5 is $\tau_{\text{prop}} = 6.2 \times 10^5$ s = 7 days. An internal wave with a dissipation time scale shorter than its propagation time scale indicates local dissipation of the wave. If the propagation time scale is less than the dissipating time scale, we expect that the dissipation of the wave is remote.

5. Results

All the identified internal waves and their properties are individually listed in Table 2. In theory,

[1] For an internal wave with a peak in the CW rotary spectra, the horizontal wave vector components (k, l) would be $k = k_h \sin(\phi)$ and $l = -k_h \cos(\phi)$.

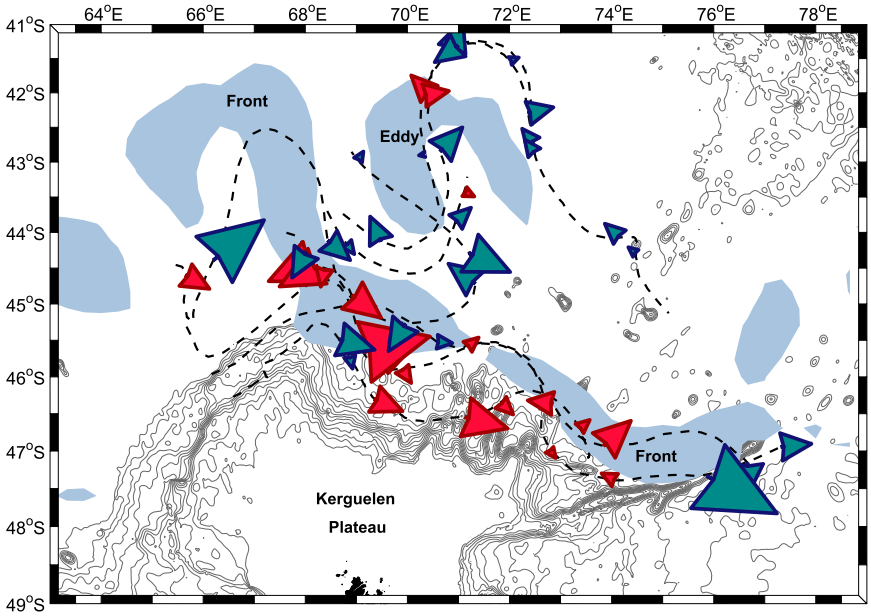

FIG. 6. Properties of the propagation and location of internal waves over topographic contours (gray). The arrow size is proportional to the horizontal intrinsic group velocity of the wave (larger arrows correspond to larger group velocities) and its color indicates the energy propagation direction (red is upward; blue is downward). Also indicated is the mean location of the SAF/STF region and the eddy during the sampling period (blue shading), corresponding to mean surface geostrophic speeds larger than 0.38 m s^{-1} between 18 Nov 2008 and the 30 Jan 2009. Topographic contours range from 600 to 3200 m at 200-m intervals. The black dashed lines indicate the trajectories of the eight EM-APEX floats.

this analysis only applies to single linear internal waves.

a. General properties of internal waves

We observe 50 internal waves in the data from the EM-APEX floats, of which numbers 1, 2, 4, and 14 have ambiguous spectral signals and are discarded. On average, eight vertical profiles of horizontal velocity define the internal waves. The internal waves are scattered along the trajectories of the floats, with most internal waves located near the northern edge of the Kerguelen Plateau, in the SAF/STF region, and in the eddy (Fig. 6). The location of the identified internal waves in the water column is relatively evenly distributed between 200 and 1000 m, with the maximum number of internal waves observed at 600 m depth.

The identified internal waves in the vicinity of the Kerguelen Plateau have a mean vertical wavelength λ of 200 m ($\sigma = \pm 20$), a mean horizontal wavelength λ_h of 15 km ($\sigma = \pm 0.9$), and a mean horizontal group velocity C_{gh} of 3 cm s^{-1} ($\sigma = \pm 0.3$), where the mean standard deviation σ of derived parameters is given in parentheses. Internal waves that are inertially forced at the ocean surface are expected to have intrinsic frequencies close to the local inertial frequency f. We find that the average period T is 16 h ($\sigma = \pm 0.2$), close to the local inertial period of 17 h at 45°S. The aspect ratio of ocean surface waves is typically one. Here, we find that the average aspect ratio (λ_h/λ) of the internal waves is 0.015 (Fig. 7a). Internal waves with a smaller period (higher frequency) have higher horizontal group velocity (Fig. 7b).

Of the 46 internal waves analyzed, 20 have energy propagating upward and 26 have energy propagating downward (Fig. 6). Downward-propagating internal waves travel in all directions, but upward-propagating internal waves have a tendency to propagate southeast on the horizontal plane (not shown). Internal waves with upward energy propagation are on average 100 m deeper than internal waves with downward energy propagation and appear clustered in the southern range of the sampling area (higher latitudes), closer to the Kerguelen Plateau, while internal waves with downward energy propagation are mostly located away from the plateau (lower latitudes). Deeper internal waves, where deep is defined as between 750 and 1200 m, propagate 25% faster than shallow waves that are shallower than 550 m depth.

The observed deep upward-propagating internal waves closer to the Kerguelen Plateau could be generated at the seafloor through the interaction of the flow

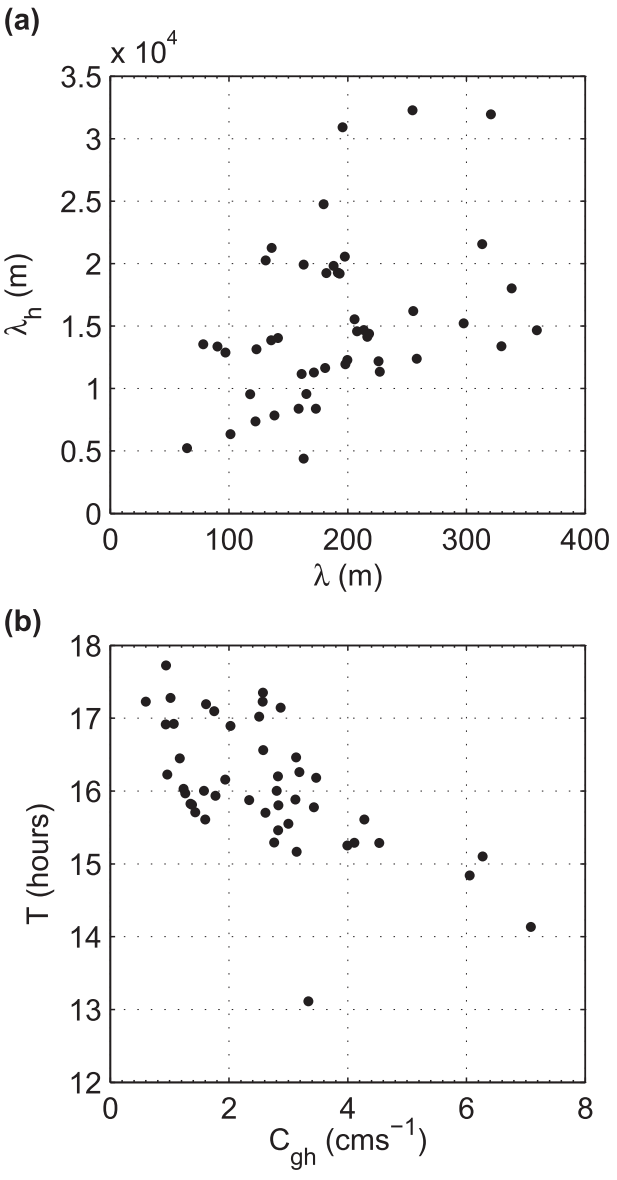

FIG. 7. (a) Ratio of λ_h/λ presents the relationship between the vertical wavelength λ and the horizontal wavelength λ_h. (b) Relationship between the horizontal group velocity C_{gh} and the period T of each of the 46 internal waves.

(either the Antarctic Circumpolar Current or tidal) and rough topography. Downward-propagating internal waves can be wind generated but can also be the result of background wave field internal waves that have been refracted, for example, in a critical layer situation or in the case of internal wave capture (Polzin 2008).

For each internal wave, we estimate the topographic roughness of the seafloor below the wave as the variance of bottom height. The topographic roughness is computed over a 0.1° longitude × 0.1° latitude box, which is approximately 8 km × 11 km, using the topography dataset from Smith and Sandwell (1997, version 13.1).[2] For each internal wave, we also estimate the associated mean wind speed within a 24-h time scale and a radius of 0.5° around the location of the wave. The wind data are a blended, satellite-derived 6-hourly wind product provided by European Remote Sensing Satellite Processing and Archiving Facility at the French Research Institute for Exploitation of the Sea.[3] Finally, we estimate the mean shear-to-strain variance ratio R_ω. These estimates are based on the results from a shear-strain finescale parameterization analysis applied to this EM-APEX dataset (Meyer et al. 2015). Variance ratio R_ω is an estimate of the mean aspect ratio of the internal wave field from which a measure of the bulk frequency of the wave field content can be derived (Polzin et al. 2014). Higher R_ω values imply a dominant presence of near-inertial waves, while lower R_ω values can be attributed to the presence of more high-frequency internal waves at high vertical wavenumber or the presence of shear instabilities when $m > m_c$ (Polzin et al. 2003).

b. *Regional characteristics of internal waves*

To identify the potential dynamics behind the generation of the observed internal waves, we separate the internal waves by their location: either in the Polar Front Zone, SAF/STF region, eddy, or Subantarctic Zone. Median values of parameters of observed internal waves and other associated parameters for each dynamical region are summarized in Table 3.

Most of the internal waves in the Polar Front Zone are propagating upward, while all of the internal waves in the Subantarctic Zone are propagating downward. Internal waves are on average deepest in the Polar Front Zone and shallowest in the Subantarctic Zone. The shortest horizontal wavelengths are on average observed in the SAF/STF region. Internal waves found in both the eddy and in the Subantarctic Zone have a period close to the local inertial period of 17 h.

Mean horizontal group velocities are higher in the Polar Front Zone [$C_{gh} = 3\,\mathrm{cm\,s^{-1}}$ ($\sigma = \pm 0.3$)] and in the eddy [$C_{gh} = 3\,\mathrm{cm\,s^{-1}}$ ($\sigma = \pm 0.3$)], but they are particularly low in the Subantarctic Zone [$C_{gh} = 1\,\mathrm{cm\,s^{-1}}$ ($\sigma = \pm 0.3$)]. We find that waves in the Polar Front Zone, where the topographic roughness is the highest, are associated with the highest percentage of upward propagating waves and the largest dissipation time scale. The internal waves in the SAF/STF region also have the highest local dissipation rate and the lowest local

[2] http://topex.ucsd.edu/WWW_html/mar_topo.html.
[3] ftp://ftp.ifremer.fr/ifremer/cersat/products/gridded/mwf-blended/data/6-hourly/.

TABLE 3. Median values of parameters of observed internal waves and other associated parameters for each dynamical region. The topographic roughness estimates are based on topography data from Smith and Sandwell (1997, version 13.1). The wind speed estimates are based on a blended satellite-derived wind product provided by the European Remote Sensing Satellite Processing and Archiving Facility at the French Research Institute for Exploitation of the Sea. The rotary-with-depth shear variance (ϕ_{CCW}/ϕ_{CW}), the shear-to-strain variance ratio R_ω, and the dissipation rate estimates result from a shear-strain finescale parameterization applied to the EM-APEX dataset in Meyer et al. (2015). The mean standard deviation σ of derived parameters is indicated in parentheses.

Parameter	Polar Front Zone	SAF/STF region	Eddy	Subantarctic Zone
Number of internal waves	17	13	13	3
Upward propagating waves (%)	71	38	23	0
Depth of wave (m)	800	700	500	600
Vertical wavelength (m; $\sigma = \pm 20$)	226	170	182	131
Horizontal wavelength (km; $\sigma = \pm 0.9$)	15	12	18	17
Period (hours; $\sigma = \pm 0.2$)	16	16	17	17
Doppler shift over f (rad; $\sigma = \pm 0.006$)	0.4	1.8	0.7	0.4
Horizontal group velocity (cm s^{-1}; $\sigma = \pm 0.3$)	3	2	2	1
Dissipation time scale (days; $\sigma = \pm 8$)	20	18	10	10
Propagation time scale (days; $\sigma = \pm 0.9$)	6	7	7	17
Topographic roughness (m^2)	15 000	10 500	6000	8500
Wind speed (m s^{-1})	7	8	8	10
Mean flow speed (m s^{-1})	0.2	0.4	0.4	0.2
ϕ_{CCW}/ϕ_{CW}	1	2	2	2
R_ω	6	5	7	7
Dissipation (W kg^{-1}; $\times 10^{-10}$)	4	15	6	1

shear-to-strain ratio (R_ω, Table 3). In the eddy, internal waves are observed at the shallowest depth, mostly downward propagating and associated with relatively high local dissipation values. In the Subantarctic Zone, where the mean wind speed is the highest, the observed internal waves all propagate downward and are relatively shallow, slow, associated with high R_ω values, and associated with the lowest local dissipation values (Table 3). We find that internal waves in the eddy and in the Subantarctic Zone areas are shallower and have intrinsic frequencies closer to the local inertial frequency f. Waves in the SAF/STF region and in the Polar Front Zone are deeper and have higher vertical wavelength.

This suggests that in the SAF/STF region, the interaction of the topography and the strong flow generates upward-propagating internal waves associated with very large values of energy dissipation. Away from the Kerguelen Plateau in the Subantarctic Zone, wind forcing might be the source of downward-propagating, near-inertial internal waves associated with smaller values of energy dissipation.

c. *Doppler shift*

The Doppler shift of the flow, $\mathbf{k} \cdot \overline{\mathbf{U}}$, impacts the propagation of internal waves (section 4f). It modifies the orientation of the wave with regard to the flow: large Doppler shifts will lead to the filamentation of an internal wave in the same manner as a passive tracer will be filamented when the rate of strain exceeds the relative vorticity (Bühler and McIntyre 2005; Polzin 2008). The rate of strain and vorticity are both spatial gradients of the advecting field. The filamentation process tends to reduce the angle between the horizontal wave vector and the flow gradients. Thus, for large Doppler shift, small angles between the flow and the wave vector are expected.

A ratio of Doppler shift to f equal to or larger than one suggests the Doppler shift is significant for that internal wave. We find that the Doppler shift is significant in the SAF/STF region, as well as in the eddy, while it is low in the Subantarctic Zone (Table 3). We estimate the orientation of the internal waves with regard to the flow gradient as the angular displacement between the horizontal wave vector and horizontal velocity vector of the local flow (Fig. 8). Angular displacements close to 90° indicate the internal wave is perpendicular to the flow while angular displacements close to 0° or 180° indicate the internal wave is parallel to the flow. We find that particularly large Doppler shift to f ratios are associated with internal waves parallel to the flow (median angle is 30°) while small Doppler shift to f ratios are associated with internal waves near perpendicular to the flow (median angle is 70°; Fig. 8). This confirms that the filamentation process associated with a large Doppler shift reduces the angle between the horizontal wave vector and the flow gradients.

d. *Internal wave and mixing fields*

We compare the location of the identified internal waves with the local mixing distribution as estimated from a shear-strain finescale parameterization (Meyer et al. 2015). Large-amplitude internal waves are likely associated with large vertical shears leading to large dissipation rates under the assumptions of the finescale

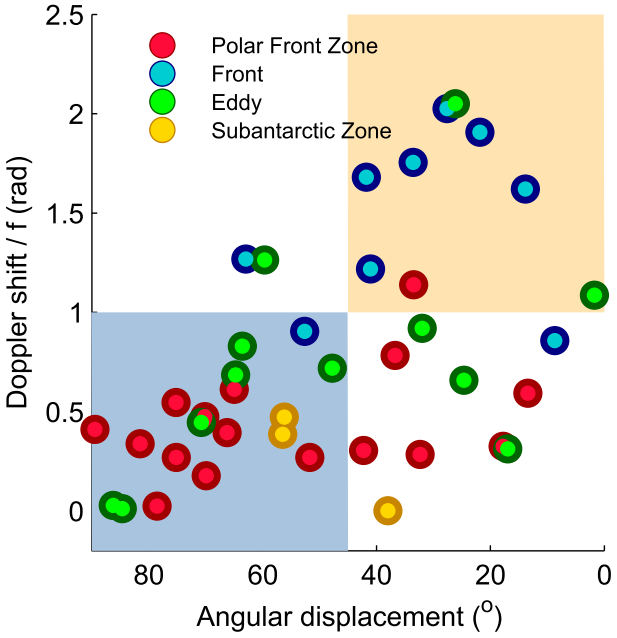

FIG. 8. Angular displacement (°) between the azimuth of the waves and the flow azimuth vs Doppler shift to f ratio for each internal wave. Internal waves with angular displacements close to 90° (waves are perpendicular to the flow) and with Doppler shift to f ratio smaller than 1 are likely affected by relative vorticity (blue shading); internal waves with angular displacements close to 0° (waves are parallel to flow) and with Doppler shift to f ratio larger than 1 are likely dominated by the Doppler shift (orange shading). The colors denote the dynamical zone to which the internal waves belong.

parameterization (Meyer et al. 2015). Since most of the internal waves observed in the EM-APEX dataset have large wave amplitudes necessary for their identification, we expect the position of observed internal waves (blue and red arrows) to match areas of enhanced dissipation rate (color contour; Fig. 9). Nearly all observed waves are found in areas where finescale parameterization predicts higher dissipation values. This confirms that the identification of internal waves is consistent with the shear-strain parameterization analysis.

6. Discussion

a. Doppler shift and relative vorticity

The EM-APEX data show that Doppler shift dynamics dominate in the SAF/STF region. Internal waves associated with large Doppler shift values tend to be aligned with the flow, while some internal waves perpendicular to the flow are associated with small Doppler shift to f ratios (Fig. 8). The latter is a characteristic of near-inertial wave trapping (Kunze 1985) where the relative vorticity gradient dominates the wave dynamics. Some internal waves in the Polar Front Zone and in the eddy are likely candidates for waves influenced by relative vorticity.

The local Doppler shift becomes dominant when it is at least half the value of the local relative vorticity (Kunze 1985; Polzin 2008). We estimate the local weekly mean vertical component of the relative vorticity ζ (s^{-1}):

$$\zeta = \left(\frac{\partial v}{\partial x} - \frac{\partial u}{\partial y}\right), \tag{25}$$

where u and v are the components of the horizontal velocity vector in the zonal and meridional from satGEM velocity fields. We set the horizontal scales to $\partial x = \partial y =$ 50 km and regrid the satGEM velocity fields onto those scales. The resulting smoothed weekly maps of mean relative vorticity show strong variability in the relative vorticity with values ranging from $-3.1 \times 10^{-5}\,s^{-1}$ to $3.1 \times 10^{-5}\,s^{-1}$ with a mean of $0.6 \times 10^{-5}\,s^{-1}$ (not shown). Estimates of the Doppler shift for each internal wave are 10–20 times larger, ranging from -40×10^{-5} to $74 \times 10^{-5}\,s^{-1}$ with a mean of $11 \times 10^{-5}\,s^{-1}$ ($\sigma = \pm 0.006$). These estimates suggest that, overall, Doppler shift processes dominate over relative vorticity. Higher-resolution estimates of the relative vorticity gradient would allow us to confirm whether Doppler shift or relative vorticity dominate individual waves and dynamical regions. In flows with little zonal symmetry and therefore with strong Doppler shift dynamics, additional modes of wave–mean interactions allow the transfer of wave momentum and the damping of the mean flow. Areas where the magnitude of the Doppler shift is large compared to the magnitude of the relative vorticity could indicate that the coupling of mesoscale eddies and internal waves discussed in Polzin (2008) and Polzin (2010) is more important than near-inertial wave trapping.

b. Wave–mean flow interactions

To investigate how much the internal waves interact with the mean flow based on their location, we analyze the spatial distribution of the dissipation time scale τ_ε and propagation time scale τ_{prop} of each wave. We find that, on average, internal waves propagate away faster than they dissipate in the SAF/STF region and in the Polar Front Zone, while in the Subantarctic Zone internal waves are likely to dissipate faster than they propagate (Table 3). Studying individual waves, we find that some internal waves in the SAF/STF region are unstable enough to dissipate locally, while other internal waves are advected away by the mean flow (Fig. 10).

This local versus far-field dissipation of internal waves has implications for the Southern Ocean stratification. That some internal waves propagate in the SAF/STF region implies they dissipate downstream, driving far-field

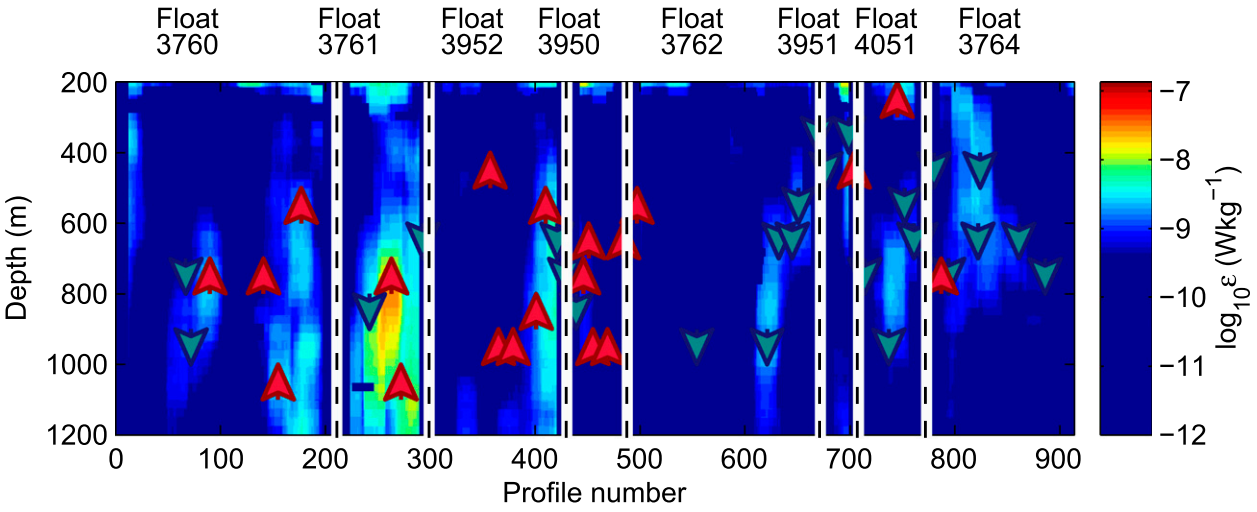

FIG. 9. Distribution of the dissipation rate ε along float trajectory estimated from the EM-APEX floats with a shear-strain finescale parameterization (Meyer et al. 2015). The overlaying arrows indicate both the location of the identified internal waves and the direction of wave propagation where red is upward and blue is downward. The vertical dashed lines separate floats.

mixing. The EM-APEX dataset strongly indicates some internal wave energy is advected away from the Kerguelen Plateau, thereby enhancing mixing and affecting the ocean stratification downstream.

7. Conclusions

The EM-APEX dataset provides a unique view of the spatial distribution and variability of the internal wave field north of the Kerguelen Plateau. Analyzing the internal waves in multiple dimensions (wavenumber and frequency domain) but also resolving the variability in the temporal and vertical wavenumber domain allows for an increasingly sophisticated characterization of the internal wave field. The results from the analysis of 46 internal waves in the area are consistent with the mixing analysis of the same dataset (Meyer et al. 2015). The high sampling density of the EM-APEX floats in space and time over a range of dynamical regions considerably enhances the information in terms of the generation and propagation of observed internal waves.

Internal waves observed near the Kerguelen Plateau have on average a vertical wavelength of 200 m (σ = ±20), a horizontal wavelength of 15 km (σ = ±0.9), a period of 16 h (σ = ±0.2) close to the local inertial period, and a horizontal group velocity of 3 cm s^{-1} (σ = ±0.3). We plan to apply ray tracing theory to estimate the temporal evolution of the wavenumber and frequency of the observed internal waves. This would provide key evidence about the sources of the internal waves identified in this dataset.

The internal wave properties, their location, and their direction of propagation are dependent on regional dynamics, suggesting that different generation mechanisms of internal waves dominate in different dynamical zones. The wave field in the SAF/STF region and the Polar Front Zone is influenced by the local small-scale topography and flow strength; the eddy-wave field is influenced by the large-scale flow structure, while the internal wave field in the Subantarctic Zone is influenced by atmospheric forcing. The SAF/STF region has an energetic wave field with the local dissipation rate associated with the waves at least twice as high as anywhere else in the area.

The analysis of the internal wave properties has far-reaching implications. We find evidence that in the SAF/STF region, only some of the internal waves generated at the Kerguelen Plateau dissipate their energy locally. Other internal waves are advected away from the region and their energy is dissipated far from the generation site. This far-field dissipation is important in setting the Southern Ocean stratification and driving the overturning circulation of the Southern Ocean.

The observed interaction of internal waves with an eddy leads to questions about energy transfers between internal waves and eddies, ultimately leading to the dissipation of internal wave energy in the form of mixing. Regions of enhanced, large-amplitude eddy activity are found in the Southern Ocean (Chelton et al. 2011). Because of the transfer of energy from internal waves to eddies, such regions have the potential to be hot spots of water mass transformation and to impact the regional overturning circulation. With the predicted intensification of wind stress and potential increase of eddy energy in the Southern Ocean over the coming decades (Meredith and Naveira Garabato 2012), it remains an open question if the eddy contribution to the mixing will increase as well.

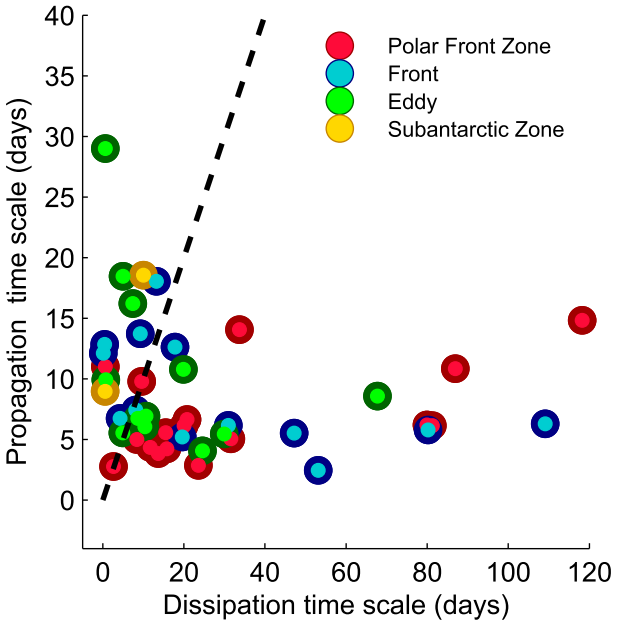

FIG. 10. Dissipation (τ_ε) and propagation (τ_{prop}) time scales of the observed internal waves. The colors denote the dynamical zone to which the internal waves belong. Waves under the black dashed line (1:1 ratio) are more likely to propagate away from the site, while waves above are more likely to dissipate locally.

We have shown that the local generation of internal waves is likely impacting the large-scale stratification of the Southern Ocean. Whether the observed internal waves are controlled by Doppler shift dynamics or relative vorticity dynamics has consequences for the regional divergence of momentum and therefore the Southern Ocean momentum balance. The role of the frontal region is key in advecting internal wave energy and momentum away from the generation site.

Acknowledgments. We thank the scientists and crew from the RRS *James Cook* JC029. We acknowledge the valuable contributions of the SOFine team, Stephanie Waterman and Alberto Naveira Garabato in particular, for providing advice and data on numerous occasions. Comments and suggestions from Beatriz Pena-Molino are gratefully acknowledged. A.M. was supported by the joint CSIRO-University of Tasmania Quantitative Marine Science (QMS) program and the 2009 CSIRO Wealth from Ocean Flagship Collaborative Fund. K.L.P.'s salary support was provided by Woods Hole Oceanographic Institution bridge support funds. B.M.S. was supported by the Australian Climate Change Science Program. We thank John Dunlap, Steve Rintoul, Susan Wijffels, and Beck Owens for their support in mounting the EM-APEX component of the SOFine project. Funding for the EM-APEX experiment was provided by the Australian Research Council Discovery Project (DP0877098) and Australian Government DEWHA Projects 3002 and 3228.

APPENDIX A

Polarization Relations

To interpret the horizontal azimuth of the horizontal wave vector φ in terms of the observed phase of the rotary velocity component ϕ, we first define the horizontal azimuth of the wave vector:

$$\tan\varphi = \frac{l}{k}. \tag{A1}$$

In the case of CCW velocity component rotation,

$$k = k_h \sin\phi, \quad \text{and} \tag{A2}$$

$$l = -k_h \cos\phi, \tag{A3}$$

and so

$$\tan\varphi = \frac{-\cos\phi}{\sin\phi}, \quad \text{and} \tag{A4}$$

$$\varphi = \tan^{-1}\frac{-\cos\phi}{\sin\phi}. \tag{A5}$$

In the case of CW velocity component rotation,

$$k = k_h \sin\phi, \quad \text{and} \tag{A6}$$

$$l = k_h \cos\phi, \tag{A7}$$

and so

$$\tan\varphi = \frac{-\cos\phi}{-\sin\phi}, \quad \text{and} \tag{A8}$$

$$\varphi = \tan^{-1}\frac{-\cos\phi}{-\sin\phi}. \tag{A9}$$

APPENDIX B

Group Velocity Approximations

The group velocity $\mathbf{C}_g$ is the gradient of the intrinsic frequency in the vertical wavenumber space:

$$\mathbf{C}_g = \left[\frac{k(N^2-\omega_0^2)^2}{\omega_0 m^2(N^2-f^2)}, \frac{l(N^2-\omega_0^2)^2}{\omega_0 m^2(N^2-f^2)}, -\frac{(\omega_0^2-f^2)(N^2-\omega_0^2)}{\omega_0 m(N^2-f^2)}\right]. \tag{B1}$$

Under the hydrostatic approximation where $\omega_0 \leq N$, and assuming $f \leq N$,

$$\mathbf{C}_g \simeq \left[\frac{kN^2}{\omega_0 m^2 N^2}, \frac{lN^2}{\omega_0 m^2 N^2}\right], \tag{B2}$$

so that

$$\mathbf{C}_g \simeq \left[\frac{kN^2}{\omega_0 m^2}, \frac{lN^2}{\omega_0 m^2}\right]. \tag{B3}$$

APPENDIX C

The WKB Approximation

The WKB approximation is used to obtain an approximate solution to a time-independent, one-dimensional differential equation. It involves recasting the wave function as an exponential power series to recover approximate solutions for the wave phase with slowly varying amplitude. The problem was first solved by Lord Rayleigh (Rayleigh 1912). Subsequently, the solution was rediscovered almost simultaneously by Wentzel (1926), Kramers (1926) and Brillouin (1926).

In oceanography, the WKB approximation is often used to limit the statistical inhomogeneity associated with varying stratification (e.g., Leaman and Sanford 1975; Müller et al. 1986; Henyey et al. 1986; Alford 2001; Polzin 2008; Sun and Pinkel 2012; Klymak et al. 2013). We apply a WKB scaling of the vertical coordinates where a mean profile of the buoyancy frequency $N(z)$ defines the WKB-stretched depth (z_{WKB}):

$$z_{\mathrm{WKB}} = \frac{1}{N_0}\int_0^z N(z)\,dz. \tag{C1}$$

The value $N_0 = 3\,\mathrm{cph}$ is the reference N (Garrett and Munk 1972). A WKB scaling is also applied to other variables such as the wavenumber and wavelength.

REFERENCES

Alford, M. H., 2001: Internal swell generation: The spatial distribution of energy flux from the wind to mixed layer near-inertial motions. *J. Phys. Oceanogr.*, **31**, 2359–2368, doi:10.1175/1520-0485(2001)031<2359:ISGTSD>2.0.CO;2.

——, M. F. Cronin, and J. M. Klymak, 2012: Annual cycle and depth penetration of wind-generated near-inertial internal waves at Ocean Station Papa in the northeast Pacific. *J. Phys. Oceanogr.*, **42**, 889–909, doi:10.1175/JPO-D-11-092.1.

Alpers, W., 1985: Theory of radar imaging of internal waves. *Nature*, **314**, 245–247, doi:10.1038/314245a0.

Apel, J. R. B., H. M. Proni, and R. L. Charnell, 1975: Observations of oceanic internal and surface waves from the Earth resource technology satellite. *J. Geophys. Res.*, **80**, 865–881, doi:10.1029/JC080i006p00865.

Belkin, I. M., and A. L. Gordon, 1996: Southern Ocean fronts from the Greenwich meridian to Tasmania. *J. Geophys. Res.*, **101**, 3675–3696, doi:10.1029/95JC02750.

Brillouin, L., 1926: Remarques sur la mecanique ondulatoire. *J. Phys.*, **7**, 353–368.

Bühler, O., and M. E. McIntyre, 2005: Wave capture and wave-vortex duality. *J. Fluid Mech.*, **534**, 67–95, doi:10.1017/S0022112005004374.

Cairns, J. L., and G. O. Williams, 1976: Internal wave observations from a midwater float, 2. *J. Geophys. Res.*, **81**, 1943–1950, doi:10.1029/JC081i012p01943.

Chelton, D., R. de Szoeke, M. Schlax, K. El Naggar, and N. Siwertz, 1998: Geographical variability of the first baroclinic Rossby radius of deformation. *J. Phys. Oceanogr.*, **28**, 433–460, doi:10.1175/1520-0485(1998)028<0433:GVOTFB>2.0.CO;2.

——, M. G. Schlax, and R. M. Samelson, 2011: Global observations of nonlinear mesoscale eddies. *Prog. Oceanogr.*, **91**, 167–216, doi:10.1016/j.pocean.2011.01.002.

Cuypers, Y., X. L. Vaillant, J. Vialard, and M. J. McPhaden, 2013: Tropical storm-induced near-inertial internal waves during the Cirene experiment: Energy fluxes and impact on vertical mixing. *J. Geophys. Res. Oceans*, **118**, 358–380, doi:10.1029/2012JC007881.

Da Silva, J. C. B., J. M. Magalhães, T. Gerkema, and L. R. M. Maas, 2012: Internal solitary waves in the Red Sea. *Oceanography*, **25**, 96–107, doi:10.5670/oceanog.2012.45.

Damerell, G. M., K. J. Heywood, and D. P. Stevens, 2013: Direct observations of the Antarctic circumpolar current transport on the northern flank of the Kerguelen Plateau. *J. Geophys. Res. Oceans*, **118**, 1333–1348, doi:10.1002/jgrc.20067.

D'Asaro, E. A., and M. D. Morehead, 1991: Internal waves and velocity fine structure in the Arctic Ocean. *J. Geophys. Res.*, **96**, 12 725–12 738, doi:10.1029/91JC01071.

——, and R. C. Lien, 2000: The wave-turbulence transition for stratified flows. *J. Phys. Oceanogr.*, **30**, 1669–1678, doi:10.1175/1520-0485(2000)030<1669:TWTTFS>2.0.CO;2.

Dosser, H. V., L. Rainville, and J. M. Toole, 2014: Near-inertial internal wave field in the Canada basin from ice-tethered profilers. *J. Phys. Oceanogr.*, **44**, 413–426, doi:10.1175/JPO-D-13-0117.1.

Fer, I., R. Skogseth, and F. Geyer, 2010: Internal waves and mixing in the marginal ice zone near the Yermak Plateau. *J. Phys. Oceanogr.*, **40**, 1613–1630, doi:10.1175/2010JPO4371.1.

Fofonoff, N. P., 1969: Spectral characteristics of internal waves in the ocean. *Deep-Sea Res.*, **16** (Suppl.), 58–71.

Forryan, A., A. C. N. Garabato, K. L. Polzin, and S. Waterman, 2015: Rapid injection of near-inertial shear into the stratified upper ocean at an Antarctic Circumpolar Current front. *Geophys. Res. Lett.*, **42**, 3431–3441, doi:10.1002/2015GL063494.

Fu, L. L., and B. Holt, 1982: SEASAT views oceans and sea ice with synthetic aperture radar. JPL Publ. 81-120, California Institute of Technology, 200 pp.

Garrett, C., and W. H. Munk, 1972: Oceanic mixing by breaking internal waves. *Deep-Sea Res. Oceanogr. Abstr.*, **19**, 823–832, doi:10.1016/0011-7471(72)90001-0.

——, and ——, 1975: Space-time scales of internal waves: Progress report. *J. Geophys. Res.*, **80**, 291–297, doi:10.1029/JC080i003p00291.

Gill, A. E., 1982: Gravity waves in a rotating fluid. *Atmosphere-Ocean Dynamics*, International Geophysics Series, Vol. 30, Academic Press, 247–315.

Hennon, T. D., S. C. Riser, and M. H. Alford, 2014: Observations of internal gravity waves by Argo floats. *J. Phys. Oceanogr.*, **44**, 2370–2386, doi:10.1175/JPO-D-13-0222.1.

Henyey, F. S., J. Wright, and S. M. Flatté, 1986: Energy and action flow through the internal wave field: An eikonal approach. *J. Geophys. Res.*, **91**, 8487–8495, doi:10.1029/JC091iC07p08487.

Johnson, G. C., J. M. Toole, and N. G. Larson, 2007: Sensor corrections for Sea-Bird SBE-41CP and SBE-41 CTDs. *J. Atmos. Oceanic Technol.*, **24**, 1117–1130, doi:10.1175/JTECH2016.1.

Kantha, L. H., and C. A. Clayson, 2000: *Small Scale Processes in Geophysical Fluid Flows*. International Geophysics, Vol. 67, Academic Press, 750 pp.

Klymak, J. M., M. Buijsman, S. Legg, and R. Pinkel, 2013: Parameterizing surface and internal tide scattering and breaking on supercritical topography: The one- and two-ridge cases. *J. Phys. Oceanogr.*, **43**, 1380–1397, doi:10.1175/JPO-D-12-061.1.

Kramers, H. A., 1926: Wellenmechanik und halbzahlige Quantisierung. *Z. Phys.*, **39**, 828–840, doi:10.1007/BF01451751.

Kunze, E., 1985: Near-inertial wave-propagation in geostrophic shear. *J. Phys. Oceanogr.*, **15**, 544–565, doi:10.1175/1520-0485(1985)015<0544:NIWPIG>2.0.CO;2.

——, L. K. Rosenfeld, G. S. Carter, and M. C. Gregg, 2002: Internal waves in Monterey Submarine Canyon. *J. Phys. Oceanogr.*, **32**, 1890–1913, doi:10.1175/1520-0485(2002)032<1890:IWIMSC>2.0.CO;2.

Leaman, K. D., and T. B. Sanford, 1975: Vertical energy propagation of internal waves: Vector spectral analysis of velocity profiles. *J. Geophys. Res.*, **80**, 1975–1978, doi:10.1029/JC080i015p01975.

Levine, M., L. Padman, R. D. Muench, and J. Morison, 1997: Internal waves and tides in the western Weddell Sea: Observations from Ice Station Weddell. *J. Geophys. Res.*, **102**, 1073–1089, doi:10.1029/96JC03013.

Liu, A. K., Y. S. Chang, M.-K. Hsu, and N. K. Liang, 1998: Evolution of nonlinear internal waves in the East and South China Seas. *J. Geophys. Res.*, **103**, 7995–8008, doi:10.1029/97JC01918.

Lueck, R. G., and R. Reid, 1984: On the production and dissipation of mechanical energy in the ocean. *J. Geophys. Res.*, **89**, 3439–3445, doi:10.1029/JC089iC03p03439.

Martini, K. I., H. L. Simmons, C. A. Stoudt, and J. K. Hutchings, 2014: Near-inertial internal waves and sea ice in the Beaufort Sea. *J. Phys. Oceanogr.*, **44**, 2212–2234, doi:10.1175/JPO-D-13-0160.1.

McDougall, T. J., and P. M. Barker, 2014: Comment on ''Buoyancy frequency profiles and internal semidiurnal tide turning depths in the oceans'' by B. King et al. *J. Geophys. Res. Oceans*, **119**, 9026–9032, doi:10.1002/2014JC010066.

Meijers, J. S., N. L. Bindoff, and S. R. Rintoul, 2011: Estimating the four-dimensional structure of the Southern Ocean using satellite altimetry. *J. Atmos. Oceanic Technol.*, **28**, 548–568, doi:10.1175/2010JTECHO790.1.

Meredith, M. P., and A. C. Naveira Garabato, 2012: Sensitivity of the overturning circulation in the Southern Ocean to decadal changes in wind forcing. *J. Climate*, **25**, 99–110, doi:10.1175/2011JCLI4204.1.

Meyer, A., B. M. Sloyan, K. L. Polzin, H. E. Phillips, and N. L. Bindoff, 2015: Mixing variability in the Southern Ocean. *J. Phys. Oceanogr.*, **45**, 966–987, doi:10.1175/JPO-D-14-0110.1.

Müller, P., G. Holloway, F. Henyey, and N. Pomphrey, 1986: Nonlinear-interactions among internal gravity-waves. *Rev. Geophys.*, **24**, 493–536, doi:10.1029/RG024i003p00493.

——, D. Olbers, and J. Willebrand, 1978: IWEX spectrum. *J. Geophys. Res.*, **83**, 479–500, doi:10.1029/JC083iC01p00479.

Munk, W., 1981: *Evolution of Physical Oceanography*. MIT Press, 664 pp.

Naveira Garabato, A. C., 2009: RRS *James Cook* Cruise 29, 01 Nov-22 Dec 2008. Cruise Rep. 35, National Oceanography Centre, Southampton, 16 pp.

Nikurashin, M., and R. Ferrari, 2011: Global energy conversion rate from geostrophic flows into internal lee waves in the deep ocean. *Geophys. Res. Lett.*, **38**, L08610, doi:10.1029/2011GL046576.

——, and ——, 2013: Overturning circulation driven by breaking internal waves in the deep ocean. *Geophys. Res. Lett.*, **40**, 3133–3137, doi:10.1002/grl.50542.

Osborn, T. R., 1980: Estimates of the local-rate of vertical diffusion from dissipation measurements. *J. Phys. Oceanogr.*, **10**, 83–89, doi:10.1175/1520-0485(1980)010<0083:EOTLRO>2.0.CO;2.

Phillips, H. E., and N. L. Bindoff, 2014: On the nonequivalent barotropic structure of the Antarctic Circumpolar Current: An observational perspective. *J. Geophys. Res. Oceans*, **119**, 5221–5243, doi:10.1002/2013JC009516.

Phillips, O. M., 1977: *The Dynamics of the Upper Ocean.* Cambridge University Press, 344 pp.

Pollard, R. T., and R. C. Millard, 1970: Comparison between observed and simulated wind-generated inertial oscillations. *Deep-Sea Res. Oceanogr. Abstr.*, **17**, 813–821, doi:10.1016/0011-7471(70)90043-4.

Polzin, K. L., 2008: Mesoscale eddy-internal wave coupling. Part I: Symmetry, wave capture, and results from the Mid-Ocean Dynamics Experiment. *J. Phys. Oceanogr.*, **38**, 2556–2574, doi:10.1175/2008JPO3666.1.

——, 2010: Mesoscale eddy-internal wave coupling. Part II: Energetics and results from PolyMode. *J. Phys. Oceanogr.*, **40**, 789–801, doi:10.1175/2009JPO4039.1.

——, and Y. V. Lvov, 2011: Toward regional characterizations of the oceanic internal wavefield. *Rev. Geophys.*, **49**, RG4003, doi:10.1029/2010RG000329.

——, E. Kunze, J. M. Toole, and R. W. Schmitt, 2003: The partition of finescale energy into internal waves and subinertial motions. *J. Phys. Oceanogr.*, **33**, 234–248, doi:10.1175/1520-0485(2003)033<0234:TPOFEI>2.0.CO;2.

——, A. C. Naveira Garabato, T. N. Huussen, B. M. Sloyan, and S. N. Waterman, 2014: Finescale parameterizations of turbulent dissipation. *J. Geophys. Res. Oceans*, **119**, 1383–1419, doi:10.1002/2013JC008979.

Rayleigh, L., 1912: On the propagation of waves through a stratified medium, with special reference to the question of reflection. *Proc. Roy. Soc. London*, **A86**, 207–226, doi:10.1098/rspa.1912.0014.

Sanford, T. B., R. G. Drever, and J. H. Dunlap, 1978: A velocity profiler based on the principles of geomagnetic induction. *Deep-Sea Res.*, **25**, 183–210, doi:10.1016/0146-6291(78)90006-1.

Scott, R. B., and Y. Xu, 2009: An update on the wind power input to the surface geostrophic flow of the World Ocean. *Deep-Sea Res. I*, **56**, 295–304, doi:10.1016/j.dsr.2008.09.010.

Smith, W. H. F., and D. T. Sandwell, 1997: Global sea floor topography from satellite altimetry and ship depth soundings. *Science*, **277**, 1956–1962, doi:10.1126/science.277.5334.1956.

Stanton, T. P., and L. A. Ostrovsky, 1998: Observations fo highly nonlinear solitons over the continental shelf. *Geophys. Res. Lett.*, **25**, 2695–2698, doi:10.1029/98GL01772.

Sun, O. M., and R. Pinkel, 2012: Energy transfer from high-shear, low-frequency internal waves to high-frequency waves near Kaena Ridge, Hawaii. *J. Phys. Oceanogr.*, **42**, 1524–1547, doi:10.1175/JPO-D-11-0117.1.

Susanto, R. D., L. Mitnik, and Q. Zheng, 2005: Ocean internal waves observed in the Lombok Strait. *Oceanography*, **18**, 80–87, doi:10.5670/oceanog.2005.08.

Thorpe, S. A., 2005: *The Turbulent Ocean.* Cambridge University Press, 439 pp.

Watanabe, M., and T. Hibiya, 2002: Global estimates of the wind-induced energy flux to inertial motions in the surface mixed layer. *Geophys. Res. Lett.*, **29**, 1239, doi:10.1029/2001GL014422.

Waterman, S., A. C. Naveira Garabato, and K. L. Polzin, 2013: Internal waves and turbulence in the Antarctic Circumpolar Current. *J. Phys. Oceanogr.*, **43**, 259–282, doi:10.1175/JPO-D-11-0194.1.

——, K. L. Polzin, A. C. Naveira Garabato, K. L. Sheen, and A. Forryan, 2014: Suppression of internal wave breaking in the Antarctic Circumpolar Current near topography. *J. Phys. Oceanogr.*, **44**, 1466–1492, doi:10.1175/JPO-D-12-0154.1.

Wentzel, G., 1926: Eine Verallgemeinerung der Quantenbedingungen für die Zwecke der Wellen-mechanik. *Z. Phys.*, **38**, 518–529, doi:10.1007/BF01397171.

Wong, A., R. Keeley, and T. Carval, 2013: Argo quality control manual, version 2.9. ARGO, 54 pp. [Available online at http://www.argodatamgt.org/content/download/20685/142877/file/argo-quality-control-manual_version2.9.pdf.]

Wunsch, C., and R. Ferrari, 2004: Vertical mixing, energy, and the general circulation of the oceans. *Annu. Rev. Fluid Mech.*, **36**, 281–314, doi:10.1146/annurev.fluid.36.050802.122121.

Zhao, Z., M. H. Alford, and J. B. Girton, 2012: Mapping low-mode internal tides from multisatellite altimetry. *Oceanography*, **25**, 42–51, doi:10.5670/oceanog.2012.40.

Zheng, Q., V. Klemas, and X. H. Yan, 2002: Advance in studies of ocean internal waves observed from space. *Recent Res. Dev. Geophys.*, **4**, 143–156.

Ziegenbein, J., 1970: Spatial observations of short internal waves in the Strait of Gibraltar. *Deep-Sea Res. Oceanogr. Abstr.*, **17**, 867–875, doi:10.1016/0011-7471(70)90004-5.